

# Initialization-Aware Score-Based Diffusion Sampling

Tiziano Fassina<sup>1</sup> Gabriel Cardoso<sup>1</sup> Sylvan Le Corff<sup>2</sup> Thomas Romary<sup>1</sup>

## Abstract

Score-based generative models (SGMs) aim at generating samples from a target distribution by approximating the reverse-time dynamics of a stochastic differential equation. Despite their strong empirical performance, classical samplers initialized from a Gaussian distribution require a long time horizon noising typically inducing a large number of discretization steps and high computational cost. In this work, we present a Kullback-Leibler convergence analysis of Variance Exploding diffusion samplers that highlights the critical role of the backward process initialization. Based on this result, we propose a theoretically grounded sampling strategy that learns the reverse-time initialization, directly minimizing the initialization error. The resulting procedure is independent of the specific score training procedure, network architecture, and discretization scheme. Experiments on toy distributions and benchmark datasets demonstrate competitive or improved generative quality while using significantly fewer sampling steps.

## 1. Introduction

In recent years, generative models have emerged as a cornerstone of machine learning due to their capacity to sample high-dimensional. Score-based generative models (SGMs) were introduced in their discrete form by Ho et al. (2020) and in their continuous formulation by Song et al. (2021b), building on several years of pioneering work (Sohl-Dickstein et al., 2015; Song and Ermon, 2019). Since then, they have achieved state-of-the-art performance in image and video generation, surpassing GANs, VAEs, and Normalizing Flows (Dhariwal and Nichol, 2021; Müller-

<sup>1</sup>Center for Statistics and Images, Mines Paris, PSL University, Fontainebleau, France <sup>2</sup>Sorbonne Université, Université Paris Cité, CNRS, Laboratoire de Probabilités, Statistique et Modélisation, LPSM, F-75005 Paris, France. Correspondence to: Tiziano Fassina <tiziano.fassina@minesparis.psl.eu>, Gabriel Cardoso <gabriel.victorino\_cardoso@minesparis.psl.eu>, Sylvain Le Corff <sylvain.le.corff@sorbonne-universite.fr >.

Franzes et al., 2022). Their frameworks form the foundation of Stable Diffusion (Rombach et al., 2022) and many of the

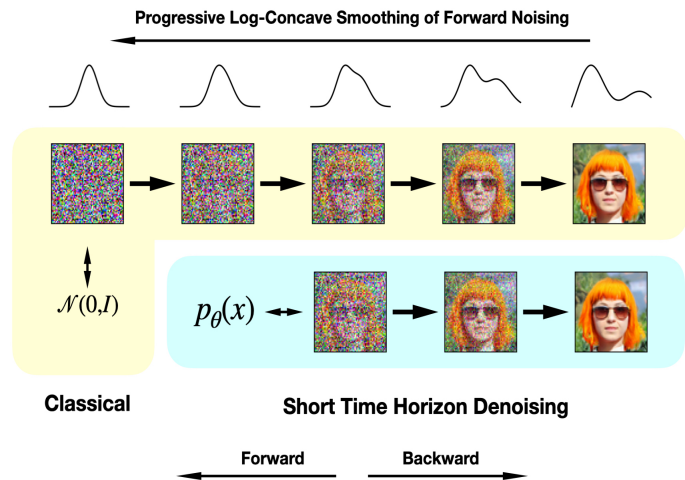


Figure 1. Comparison of sampling trajectories. Traditional SGMs sample across the full horizon  $T$  from a Gaussian, while our approach models the intermediate noise distribution, enabling short-horizon sampling that preserves generative quality and reduces computation.

most prominent publicly available models today, including DALL-E 3 (Betker et al., 2023), Imagen 3 (Baldrige et al., 2024), and recent advanced architectures like FLUX (Black Forest Labs, 2025). SGMs have also demonstrated potential and competitive results in audio (Chen et al., 2021; Kong et al., 2021) and text generation (Li et al., 2022; Zou et al., 2023). This positions SGMs as a flexible and powerful framework, offering robustness and versatility across diverse data modalities.

The core idea of SGMs is twofold. First, the data distribution is gradually corrupted by adding Gaussian noise. Second, a neural network is trained to reverse this process, estimating the noise to recover the original data sample from its corrupted version. New samples are generated by starting from standard Gaussian noise and iteratively applying the trained network to progressively denoise it.

Standard approaches add noise to the data such that the resulting noisy samples approximately follow a Gaussian distribution, which leads to several limitations. In particular, this often necessitates a long forward noising horizon,

which in practice entails a substantial computational cost due to the large number of required denoising steps. To mitigate this, several efficient sampling methods were proposed, ranging from the original DDPM sampling (Ho et al., 2020) to DDIM (Song et al., 2021a), PNDM (Liu et al., 2022), and EDM (Karras et al., 2022), which all aimed at reducing the number of steps while preserving generative quality. This also requires that the network accurately estimates the score over a large range of noise levels, which necessitates a well tailored training procedure. Accordingly, complementary research has focused on improving training efficiency through architectural and procedural strategies (Song et al., 2021b; Dhariwal and Nichol, 2021; Karras et al., 2022; 2024). In some cases, Gaussian initialization is insufficient, such as for heavy-tailed distributions, necessitating alternative solutions (Pandey et al., 2025).

While Gaussian initialization is a pillar of the SGM framework, its necessity can be challenged by observing the distribution dynamics during the forward noising process. The analysis of the forward probability densities induced by Gaussian convolution is a classical research area (Evans, 2010), and recent advances demonstrate that noising implies a rigorously controllable smoothing procedure of the data distribution. Specifically, Silveri and Ocello (2025) demonstrate that the forward noising procedure is a form of regularization that can be rigorously quantified by tracking the evolution of the log-concavity and Lipschitz constants of the data distribution.

This perspective on distribution smoothing allows us to interpret the diffusion process as a complexity reduction mechanism. By leveraging the forward process, we can identify intermediate distributions that exhibits increased regularity compared to the original data. Those simpler distributions can be efficiently approximated using appropriate and fast models, such as Normalizing Flows for images (Zhai et al., 2025; Dinh et al., 2017; Papamakarios et al., 2021), and subsequently refined through a truncated denoising trajectory. Furthermore, a rich body of literature offers significant potential for analyzing the modeling of smoothed distributions (Dalalyan, 2017; Durmus and Moulines, 2017; Gao et al., 2024; 2025).

This paper makes the following contributions.

- We present a KL-based theoretical analysis of the Variance Exploding (VE) forward and backward SDEs, extending the framework of Conforti et al. (2025) to a practically important setting that had not been previously studied. Our analysis relies on slightly weaker assumptions and decomposes the upper bound into three distinct terms corresponding to initialization, discretization, and denoising approximation errors. More importantly, the proof, carried out without relying on score normalization, clearly separates the contribution

of the initialization from the errors arising from training and discretization.

- Guided by our theoretical analysis, we introduce an efficient data-driven initialization for the VE sampler. Starting the reverse process at an intermediate noise level shortens the sampling horizon and reduces denoising steps while maintaining high sample quality. This theoretically grounded initialization allows to improve sample quality in heavy-tail settings and conditional sampling problems.
- We evaluate our method on toy distributions, benchmark datasets, and state-of-the-art architectures and samplers (2022; 2024), showing compatibility with widely used frameworks. Our approach is architecture- and sampler-agnostic, achieving competitive generative quality with lower computational cost and energy use.

## 2. Related Works

**Training intermediate distributions.** The idea that intermediate, noised distributions are easier to model has been empirically explored in the literature. Zheng et al. (2023) proposed a diffusion-based generative model that shortens the diffusion trajectory by learning, via an Adversarial Autoencoder (AAE), a prior at a truncated diffusion time that approximates the aggregated posterior of the forward noising process. In (Zand et al., 2024), the authors introduced DiNof, which uses a Glow Normalizing Flow to approximate the noised distribution at any arbitrary step of the diffusion process, thereby reducing sampling time. In addition, sample quality highlights the potential of using both SDEs on classical image datasets. Additionally, Frey et al. (2024) proposed Discrete Walk-Jump sampling, which uses two uncoupled models, a score-based model and an Energy-Based Model, employing a single noise level to stabilize EBM training and accelerate sampling via a one-step denoiser.

While these methods improve sample quality and computational efficiency in specific settings, they lack the theoretical analysis to be considered as a general, broadly applicable approach. In contrast, our method provides a unified, theoretically grounded framework that applies across architectures, samplers, and data distributions, and is compatible with several settings. Beyond emphasizing the role of the initialization in the convergence bound, we also show that our training procedure can be analyzed using recent results on the excess risk of variational estimators.

**SGM Guarantees.** To the best of our knowledge, existing theoretical works on SGMs establish convergence and error guarantees exclusively under a fixed Gaussian initial-

ization. Such guarantees are developed either within the KL-divergence framework (Conforti et al., 2025) or within the Wasserstein-distance literature (Bortoli, 2022; Strasman et al., 2025a;b; Gao et al., 2025; Bruno and Sabanis, 2025; Silveri and Ocello, 2025), and uniformly rely on this standard initialization assumption, without considering alternative initialization schemes. Our theoretical analysis focuses on the initialization error, decoupled from the training of the score model, and introduces a theoretically grounded criterion for optimizing the initialization of the backward process.

**Complementary Methods.** Flow matching methods (Lipman et al., 2023) have recently shifted focus to transport cost and toward designing informative priors (Issachar et al., 2024; Tong et al., 2024; Kornilov et al., 2024; Feng et al., 2025). For example, Issachar et al. (2024) constructs conditional priors from training-data centroids in order to improve generation. Tong et al (2024) proposes a batch algorithm for optimal transport flow matching. Our approach provides a general prior-design framework that supports both unconditional and conditional priors. By using priors closer to the target distribution, it offers the potential to shorten the transport path. Alternatively, one-step methods like Consistency Models (Song et al., 2023) and MeanFlow (Geng et al., 2025) reduce sampling time, but learning a direct map from a Gaussian prior to complex data remains challenging. Using intermediate distributions offers a promising approach for more efficient one-step trajectories.

### 3. KL Control & Short Time Diffusion

We introduce the notations and assumptions underlying our main theoretical result in Theorem 3.1. The complete proof and auxiliary lemmas are available in Section A. Let  $(\Omega, \mathcal{F}, \mathbb{P})$  be a probability space and  $L^2(\Omega, \mathcal{F}, \mathbb{P})$  the space of square-integrable random variables on  $\Omega$ . We denote by  $\mu_*$  the unknown data distribution on  $\mathbb{R}^d$ , and the goal of SGMs is to generate new samples from  $\mu_*$  given only an observed dataset.

#### 3.1. Context

**Forward process.** Score-based generative models rely on a forward noising process governed by the SDE:

$$d\vec{X}_t = -\alpha_t \vec{X}_t dt + g_t dB_t, \quad (1)$$

where  $B_t \in \mathbb{R}^d$  denotes a standard Brownian motion and  $\alpha_t, g_t : \mathbb{R}^+ \rightarrow \mathbb{R}$  are assumed to be bounded and sufficiently smooth to guarantee existence and uniqueness of solutions (Haussmann and Pardoux, 1986; Øksendal, 2003). We consider *Variance Exploding* VE diffusion (Song et al., 2021b), obtained by removing the drift term:

$$d\vec{X}_t = g_t dB_t. \quad (2)$$

Given  $\vec{X}_0 \sim \mu_*$  on  $\mathbb{R}^d$ , we consider the solution  $(\vec{X}_t)_{t \in [0, T]}$  for some fixed  $T > 0$  and we assume to ensure the existence of the process that  $\vec{X}_0 \in L^2(\Omega, \mathcal{F}, \mathbb{P})$ . We set

$$\sigma_t^2 := \int_0^t g_s ds.$$

The forward solution satisfies

$$\vec{X}_t \stackrel{\mathcal{L}}{=} \vec{X}_0 + \sigma_t Z,$$

where  $Z \sim \mathcal{N}(0, I_d)$  is independent of  $\vec{X}_0$ . The forward solution  $\vec{X}_t$  admits a density denoted by  $\vec{p}_t$  with respect to the Lebesgue measure on  $\mathbb{R}^d$ .

**Backward process.** By the time-reversal theorem, we can introduce the backward dynamics of (2) as another SDE (Haussmann and Pardoux, 1986; Song et al., 2021b). The well-posedness of the backward equation is addressed later. Letting  $\bar{g}_t := g_{T-t}$  for  $t \in [0, T]$ , the backward SDE is defined as

$$d\overleftarrow{X}_t = \bar{g}_t^2 \nabla \log \bar{p}_{T-t}(\overleftarrow{X}_t) dt + \bar{g}_t d\tilde{B}_t, \quad (3)$$

where  $\tilde{B}_t$  is an independent Brownian motion and  $\overleftarrow{X}_0 \sim p_T$ . The solution  $(\overleftarrow{X}_t)$  is well defined on any interval  $[0, T - \delta]$  for arbitrary  $\delta > 0$ , and satisfies the standard time-reversal relation: for all  $t \in [\delta, T]$ ,  $\overleftarrow{X}_t = \overleftarrow{X}_{T-t}$ . In practice,  $\mu_*$  is not available; instead, we only have access to an i.i.d. sample  $\vec{X}_0^i \sim \mu_*$ ,  $1 \leq i \leq n$ . Consequently, the solution of Equation (3) that would enable sample generation is not directly accessible, since neither the score nor the terminal distribution  $\bar{p}_T$  of the backward process are known. Furthermore, the backward SDE does not admit a closed-form solution, making it necessary to rely on discretization schemes.

For the purpose of theoretical analysis, following common practice, we may rely on either the Euler–Maruyama scheme (Gao et al., 2025; Silveri and Ocello, 2025) or the Exponential Euler–Maruyama scheme (Conforti et al., 2025; Strasman et al., 2025a). Remarkably, in the VE setting these two schemes coincide, allowing for a unified treatment of the KL bound.

**Score approximation and discretization.** By replacing the real score function  $\nabla \log \bar{p}_{T-t}$  using a trained neural network  $s_\theta(T-t, \cdot)$ , we introduce the discretized backward dynamics

$$dX_t^\theta = \bar{g}_t^2 s_\theta(T-t_k, X_{t_k}^\theta) dt + \bar{g}_t d\tilde{B}_t, \quad (4)$$

for  $t \in [t_k, t_{k+1}]$ , where  $t_{k+1} = t_k + h_{k+1}$ , with  $t_0 = 0$  and  $t_N = T - \delta$  which can be equivalently written, for

$t \in [0, T - \delta]$ , as

$$dX_t^\theta = \sum_{k=0}^{N-1} \bar{g}_t^2 s_\theta(T - t_k, X_{t_k}^\theta) \mathbf{1}_{t \in [t_k, t_{k+1}]} dt + \bar{g}_t d\tilde{B}_t. \quad (5)$$

This discretization scheme results in the following stochastic sampling dynamics:

$$X_{t_{k+1}}^\theta = (\sigma_{T-t_k}^2 - \sigma_{T-t_{k+1}}^2) s_\theta(T - t_k, X_{t_k}^\theta) + (\sigma_{T-t_k}^2 - \sigma_{T-t_{k+1}}^2) Z, \quad (6)$$

for  $k = 0, \dots, N - 1$ ,  $Z \sim \mathcal{N}(0, I_d)$ .

**Initialization of the backward sampler.** To recover the original distribution, initialization should ideally use  $\vec{p}_T$ , which is generally unavailable. Theoretical analyses of SGMs typically assume a centered Gaussian initialization with variance  $\sigma_T^2 I_d$ , denoted  $\pi_\infty$ . This distribution is used both to initialize the backward sampler and in (Conforti et al., 2025) to normalize the score in the analysis of the discretization error. In this paper, we consider a generic parametric distribution  $p_0^\theta$  to initialize the backward sampler, which forms the core of our short-time sampling method.

We introduce the notation for the Fisher information of a distribution  $\nu$ , admitting a regular density function :

$$\mathcal{I}(\nu) := \int_{\mathbb{R}^d} \left\| \nabla \log \frac{d\nu}{d\lambda_{\mathbb{R}^d}} \right\|^2 d\nu,$$

where  $\lambda_{\mathbb{R}^d}$  denotes the Lebesgue measure. When  $\mu$  and  $\nu$  are probability measures and  $\mu$  is absolutely continuous with respect to  $\nu$ , we can also define the Kullback-Leibler divergence between  $\mu$  and  $\nu$  :

$$D_{\text{KL}}(\mu || \nu) = \int \log \frac{d\mu}{d\nu}(x) \mu(dx),$$

where  $d\mu/d\nu$  is the Radon–Nikodym derivative of  $\mu$  with respect to  $\nu$ . Finally, define  $s_t(x) = \nabla \log \vec{p}_t(x)$  and for all  $1 \leq k \leq N - 1$ ,

$$\gamma_k = \int_{t_k}^{t_{k+1}} \bar{g}_t^2 dt. \quad (7)$$

### 3.2. Hypothesis & Main Result

Consider the following assumptions.

- H1**
- $\vec{X}_0 \in L^2(\Omega, \mathcal{F}, \mathbb{P})$ .
  - $t \mapsto g_t$  is in  $C^\infty([0, T], \mathbb{R}^+)$ .
  - $p_0^\theta$  and  $\lambda_{\mathbb{R}^d}$  are mutually absolutely continuous.

For all  $x \in \mathbb{R}^d$  and  $0 \leq t \leq T$ , denote by  $\vec{X}_t^x$  the solution to (3) at time  $t$  with deterministic initialization  $x$ .

**H2** Assume that for  $\lambda_{\mathbb{R}^d}$  almost all  $x \in \mathbb{R}^d$ ,

$$\mathbb{P} \left( \sum_{k=0}^{N-1} \int_{t_k}^{t_{k+1}} \frac{1}{\bar{g}_t^2} \|s_\theta(T - t_k, \vec{X}_{t_k}^x)\|^2 dt + \int_0^T \frac{1}{\bar{g}_t^2} \|\nabla \log \vec{p}_{T-t}(\vec{X}_t^x)\|^2 dt < \infty \right) = 1.$$

**H3** There exists  $\varepsilon > 0$  such that for all  $0 \leq k \leq N - 1$ ,

$$\mathbb{E} \left[ \|\nabla \log \vec{p}_{T-t_k}(\vec{X}_{t_k}) - s_\theta(T - t_k, \vec{X}_{t_k})\|^2 \right] \leq \varepsilon.$$

Hypothesis H1 is introduced to allow the existence of the forward solution and it is weaker than the eight-moment existence assumption of Conforti et al. (2025). We show in Section A that this hypothesis is also sufficient for the backward process existence in this particular case. To ensure a well-posed KL divergence at initialization, we assume  $p_0^\theta$  and  $\lambda_{\mathbb{R}^d}$  are mutually absolutely continuous. Hypothesis H2 is a technical hypothesis necessary for studying the relationship between the two backward solutions. We do not state our theorem in terms of a bound on the KL divergence between the original distribution  $\mu_*$  and  $p_T^\theta$ , because doing so would require imposing strong assumptions on  $\mu_*$ , such as absolute continuity and high regularity. Therefore, our theorem is stated in terms of the distribution  $\vec{p}_\delta$ , obtained by convolving  $\mu_*$  with a Gaussian of arbitrarily small variance  $\sigma_\delta^2$ , and the generative distribution  $p_{T-\delta}^\theta$ . Employing early stopping also lets us bypass the assumption of finite Fisher information for the data distribution, which was required in Conforti et al. (2025) and Strasman et al. (2025a). In practice this is by no means a limitation, as early stopping is commonly used in sampling (Karras et al., 2022). Consider the following additional notations: for all  $\theta, t \in [0, T]$ ,  $0 \leq k \leq N - 1$ ,

$$\begin{aligned} \mathcal{E}_\theta(t_k, \vec{X}_{t_k}) &= s_{T-t_k}(\vec{X}_{t_k}) - s_\theta(T - t_k, \vec{X}_{t_k}), \quad (8) \\ \mathcal{E}(t_k, t, \vec{X}_{t_k}, \vec{X}_t) &= s_{T-t_k}(\vec{X}_{t_k}) - s_{T-t}(\vec{X}_t). \end{aligned}$$

**Theorem 3.1.** Assume that H1-2 hold. Then, for all  $\delta > 0$ ,

$$D_{\text{KL}}(\vec{p}_\delta || p_{T-\delta}^\theta) \leq E_{\text{init}}(\theta) + E_{\text{train}}(\theta) + E_{\text{disc}},$$

with

$$E_{\text{init}}(\theta) = D_{\text{KL}}(\vec{p}_T || p_0^\theta), \quad (9)$$

$$E_{\text{train}}(\theta) = \sum_{k=0}^{N-1} \gamma_k \mathbb{E} \left[ \left\| \mathcal{E}_\theta(t_k, \vec{X}_{t_k}) \right\|^2 \right], \quad (10)$$

$$E_{\text{disc}} = \sum_{k=0}^{N-1} \int_{t_k}^{t_{k+1}} \bar{g}_t^2 \mathbb{E} \left[ \left\| \mathcal{E}(t_k, t, \vec{X}_{t_k}, \vec{X}_t) \right\|^2 \right] dt, \quad (11)$$

where  $\mathcal{E}_\theta(t_k, \overleftarrow{X}_{t_k})$  and  $\mathcal{E}(t_k, t, \overleftarrow{X}_{t_k}, \overleftarrow{X}_t)$  are defined in (8).

In addition, the term  $E_{\text{disc}}$  is upper bounded by

$$E'_{\text{disc}} = \max_{k=0, \dots, N-1} \gamma_k \{ \mathcal{I}(\vec{p}_\delta) - \mathcal{I}(\vec{p}_T) \} . \quad (12)$$

Assume in addition that H3 holds. Then,

$$D_{\text{KL}}(\vec{p}_\delta \| p_{T-\delta}^\theta) \leq D_{\text{KL}}(\vec{p}_T \| p_0^\theta) + \sigma_T^2 \epsilon + E'_{\text{disc}} . \quad (13)$$

### 3.3. KL-driven initialization learning

Theorem 3.1 decomposes the total generation error into three contributions. Achieving high-quality generation requires satisfying three key conditions:

- the **initial distribution** the Kullback-Leibler divergence between  $p_0^\theta$  and  $\vec{p}_T$  must be small;
- the **score network** must achieve low mean-square error at all timesteps;
- the **time discretization** must be fine enough to accurately approximate the continuous dynamics.

Increasing  $T$  improves alignment between  $\vec{p}_T$  and the standard Gaussian initialization  $\pi_\infty$ , but worsens the other two error terms. In particular

1. **Training difficulty.** The term  $\sigma_T^2 \epsilon$  grows directly with  $\sigma_T$ . Furthermore, large time horizon forces the network to spread its capacity across a wide noise window  $[0, T]$  potentially worsening the constant  $\epsilon$ .
2. **Fisher information gap.** The difference  $\mathcal{I}(\vec{p}_\delta) - \mathcal{I}(\vec{p}_T)$  grows directly with  $T$  damaging  $E'_{\text{disc}}$ .
3. **Scheduler effect.** For  $N$  discretization steps, each step spans  $h_k = T/N$ . Increasing  $T$  enlarges this gap still damaging  $E'_{\text{disc}}$ .

Classical diffusion uses a large noise scale  $\sigma_T$  and a long horizon  $T$  to ensure that  $\pi_\infty$  approximates  $\vec{p}_T$  correctly, reducing initialization error but increasing training and discretization errors. Our proposal is to replace the standard choice by a statistical model  $p_0^\theta$  that approximates  $\vec{p}_T$ , enabling faster and high quality short-horizon diffusion. The proposed procedure would neither be interesting nor practically feasible if the distribution  $\vec{p}_t$  did not progressively simplify as  $t \rightarrow T$ . In this regard, (Silveri and Ocello, 2025)[Lemma B.3] provides a formal characterization of the gradual increase in smoothness and log-concavity of the convolved distribution  $\vec{p}_t$ , thereby justifying the use of expressive and efficient density estimators which can accurately capture the regularized distribution geometry.

---

#### Algorithm 1 Short-Horizon Flow-Diffusion Training

---

- 1: **Input:** Dataset  $\mathcal{D} = \{\mathbf{x}_0^{(i)}\}_{i=1}^N$
  - 2: **Output:** Optimized  $p_0^\theta$
  - 3: Noisy dataset  $\mathcal{D}_T = \{\mathbf{x}_0^{(i)} + \sigma_T \mathbf{z}^{(i)}\}_{i=1}^N$   
 $\mathbf{z}^{(i)} \sim \mathcal{N}(0, \mathbf{I})$
  - 4: **for** each training iteration **do**
  - 5:   Batch  $\{\mathbf{x}_T\}$  from  $\mathcal{D}_T$
  - 6:   Gradient Descent step on  $-\log p_0^\theta(\mathbf{x}_T)$
  - 7: **end for**
- 

By Theorem 3.1, given a statistical model  $\{p_0^\theta(x)\}_{\theta \in \Theta}$ , we aim at solving

$$\theta^* \in \arg \min_{\theta \in \Theta} D_{\text{KL}}(\vec{p}_T \| p_0^\theta) = \arg \min_{\theta \in \Theta} \mathbb{E}[\mathfrak{m}(\vec{X}_T; \theta)] .$$

where

$$\mathfrak{m}(x; \theta) = \log \vec{p}_T(x) - \log p_0^\theta(x) .$$

In practice, we consider the empirical risk optimization problem

$$\hat{\theta}^n \in \arg \min_{\theta \in \Theta} \sum_{i=1}^n \mathfrak{m}(\vec{X}_T^i; \theta) = \arg \max_{\theta \in \Theta} \sum_{i=1}^n \log p_0^\theta(\vec{X}_T^i) .$$

In our experiments, we minimize the empirical risk via stochastic gradient descent as in Algorithm 1. Bounds on the excess risk  $D_{\text{KL}}(\vec{p}_T \| p_0^\theta[\hat{\theta}^n])$  depend heavily on the behavior of the tails of the target distribution, i.e.  $\vec{p}_T$  in our setting. The Orlicz norm (Wainwright, 2019)[Section 5.6] is useful for quantifying the tail properties of distributions. It is defined, for a random variable  $X$ , as

$$\|X\|_{\psi_1} = \inf \left\{ K > 0 : \mathbb{E} \left[ \exp \left( \frac{|X|}{K} \right) \right] \leq 2 \right\} .$$

**Assumption 3.2.** There exists  $D \in \mathbb{R}$  such that

$$\left\| \sup_{\theta \in \Theta} \mathfrak{m}(\vec{X}_T; \theta) \right\|_{\psi_1} \leq D . \quad (14)$$

**Assumption 3.3.**  $\Theta$  is compact and there exists  $\mathfrak{b} : \mathbb{R}^d \rightarrow \mathbb{R}_{\geq 0}$  such that for all  $x \in \mathbb{R}^d$ , and all  $(\theta, \tilde{\theta}) \in \Theta^2$ ,

$$|\mathfrak{m}(x; \theta) - \mathfrak{m}(x; \tilde{\theta})| \leq \mathfrak{b}(x) \|\theta - \tilde{\theta}\|_2 , \quad (15)$$

with  $\left\| \mathfrak{b}(\vec{X}_T) \right\|_{\psi_1} < \infty$ .

Following (Tang and Yang, 2021), Assumption 3.2 and Assumption 3.3 are enough to provide oracle inequalities on the excess risk.

**Theorem 3.4** (Adaptation of (Tang and Yang, 2021)[Theorem 3]). *Assume that Assumptions 3.2 and 3.3 hold.*

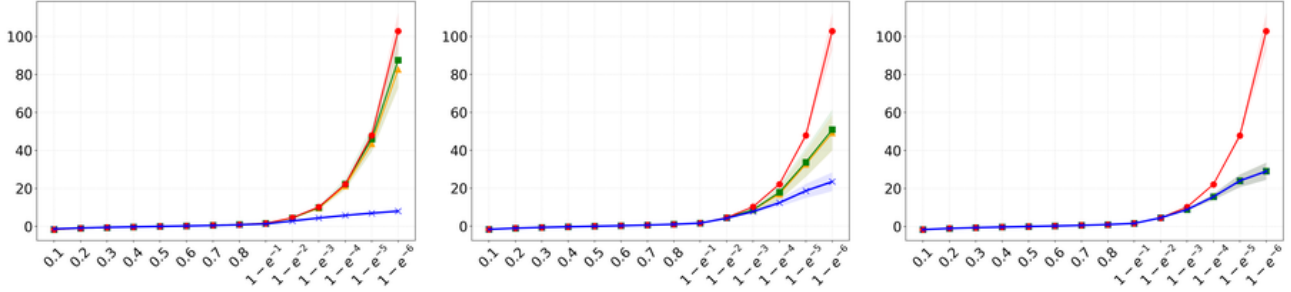


Figure 2. Quantile plot (0.1–0.999999) of mean and std over  $d = 100$  dimensions for heavy-tailed distributions:  $p_\infty$  (x),  $p_T$  ( $\blacktriangle$ ),  $p_\theta$  ( $\blacksquare$ ), real data ( $\bullet$ ). Respectively  $\sigma_T = \{2, 7, 80\}$ . On the x-axis the quantile levels, on the y-axis the quantile values.

Then, there exist some constants  $(c_0, c_1, c_2)$  such that, with probability at least  $1 - c_0 \exp(-c_1 d_\theta \log n)$ ,

$$\begin{aligned} D_{\text{KL}}(\vec{p}_T \| p_0^{\hat{\theta}^n}) &\leq \inf_{\gamma > 0} \left\{ (1 + \gamma) D_{\text{KL}}(\vec{p}_T \| p_0^{\theta^*}) \right. \\ &\quad \left. + c_2 (1 + \gamma^{-1}) \frac{D d_\theta}{n} \log(nd_\theta) \log(n) \right\}. \quad (16) \end{aligned}$$

Theorem 3.4 implies that up to logarithmic terms, the excess scales as  $1/n$ . More importantly, this is governed by  $D$ .

While we have described this procedure in a general framework that encompass parametric estimation quite generally, we provide a discussion in Section C of how it can be used to deal with inference using Normalizing flow (namely how to ensure Assumptions 3.2 and 3.3 in this case), as it is the most common example of parametric family used in the current paper. We namely detail the impact of the Orlicz norm of  $\mu_*$  and how it is propagated to the excess risk bound as a function of the diffusion time  $T$ .

## 4. Experiments

**Gaussian Mixture Model.** We evaluate the performance of our method on Gaussian Mixture Models (GMM). We draw both the Gaussian component parameters and the mixture weights randomly (details in Section B.1) yielding a 25 component mixture with non-isotropic Gaussian components. The experiments are conducted in dimensions  $d = 40$  and  $d = 100$ . We approximate  $\vec{p}_T(x)$  with  $p_0^\theta(x)$  being a RealNVP (Dinh et al., 2017) architecture which is trained by minimizing log-likelihood. Further details are given in Section B.1. To isolate the contribution of the initialization, we employ the analytically available score function.

**Heavy-tailed Distribution.** Our method also suggests potential for Heavy-tailed (HT) distributions, which are widely used to model extreme events. A variable  $W = (W_1, \dots, W_d) \in \mathbb{R}^d$  is called heavytail (see (Bingham et al., 1987) for a precise definition) if there is at least one

Table 1. MaxSWD values for GMM and HT with  $d = 40$  and 100. Reference MaxSWD values are provided in the first line of Table 11.

Dim	Model	MaxSWD		
		$\sigma_T = 2$	$\sigma_T = 7$	$\sigma_T = 80$
<b>GMM</b>				
$d = 40$	$\pi_\infty$	$5.2 \pm 0.6$	$2.1 \pm 0.1$	$0.823 \pm 0.01$
	$p_0^\theta(x)$	$0.46 \pm 0.06$	$0.49 \pm 0.01$	$0.86 \pm 0.01$
	$\vec{p}_T(x)$	$0.1 \pm 0.02$	$0.12 \pm 0.02$	$0.84 \pm 0.01$
$d = 100$	$\pi_\infty$	$5.03 \pm 0.005$	$2.129 \pm 0.005$	$0.9 \pm 0.01$
	$p_0^\theta(x)$	$0.97 \pm 0.009$	$0.56 \pm 0.01$	$0.921 \pm 0.009$
	$\vec{p}_T(x)$	$0.15 \pm 0.04$	$0.16 \pm 0.03$	$0.921 \pm 0.007$
<b>HT</b>				
$d = 40$	$\pi_\infty$	$0.88 \pm 0.201$	$0.49 \pm 0.238$	$0.428 \pm 0.287$
	$p_0^\theta(x)$	$0.327 \pm 0.226$	$0.443 \pm 0.250$	$0.428 \pm 0.287$
	$\vec{p}_T(x)$	$0.402 \pm 0.210$	$0.381 \pm 0.253$	$0.414 \pm 0.289$
$d = 100$	$\pi_\infty$	$1.265 \pm 1.281$	$0.855 \pm 1.137$	$0.793 \pm 1.152$
	$p_0^\theta(x)$	$0.586 \pm 1.193$	$0.881 \pm 1.127$	$0.792 \pm 1.153$
	$\vec{p}_T(x)$	$0.529 \pm 0.849$	$0.839 \pm 1.136$	$0.792 \pm 1.153$

$1 \leq j \leq d$  such that

$$\mathbb{P}(W_j > t) \sim t^{-\nu} \quad \text{as } t \rightarrow \infty, \quad \nu > 0.$$

Standard score-based generative models struggle with heavy tails, a difficulty partly rooted in the discrepancy between the light-tailed Gaussian initialization  $\pi_\infty$  and the noised distribution  $W + \sigma_T Z \sim \vec{p}_T$ , which remains  $\nu$ -heavy-tailed for any  $\sigma_T > 0$ . Several non-SGM approaches address heavy-tailed distributions (Allouche et al., 2022; McDonald et al., 2022; Lafon et al., 2023; Hickling and Prangle, 2025), but may inherit structural and optimization-related limitations of their underlying architectures. Existing SGM-based methods typically rely on modified noising processes (Yoon et al., 2022; Shariatian et al., 2025; Pandey et al., 2025). By using an appropriate heavy-tailed approximation of  $\vec{p}_T(x)$ , we propose an approach that improves tail coverage while retaining the standard Gaussian noising process. We test this idea in dimensions  $d = 40, 100$  on a simple multimodal

Table 2. Results for ImageNet<sub>birds</sub>

Model	FID	DINO FD	MaxWD
$\pi_\infty$ (Classic)	5.90	67.13	$5.095 \pm 0.129$
$p_0^\theta$	3.38	58.72	$1.955 \pm 0.112$
$\vec{p}_T$	3.91	53.49	$1.258 \pm 0.633$

HT distribution:

$$W = BT_1 + (1 - B)T_{-1},$$

where  $B \sim \text{Bernoulli}(1/2)$ , and  $T_{\pm 1} \sim t_\nu(\mu_{\pm 1}, \mathbf{I})$  are multivariate Student-t distributions with  $\nu = 3$  degrees of freedom and location vectors  $\mu_1 = (1/\sqrt{d}, \dots, 1/\sqrt{d})$  and  $\mu_{-1} = (-1/\sqrt{d}, \dots, -1/\sqrt{d})$ . We choose  $p_0^\theta(x)$  to be the convolution between a Student-t distribution with degrees of freedom  $\hat{\nu}$  and a Gaussian noise  $\mathcal{N}(0, \sigma_T^2 I)$ , where  $\hat{\nu}$  is estimated via the Hill estimator which is consistent and asymptotically normal under mild assumptions. In the heavy-tailed regime, classical KL minimization is often replaced by tail-index estimation to improve robustness. Unfortunately, the score function is not analytically available for HT distributions. Consequently, in this setting, we were required to train a denoiser for score estimation.

**Evaluation on synthetic datasets.** We consider time horizon  $\sigma_t = \{2, 5, 7, 15, 80\}$  for both datasets. For the GMM experiments, we used 10 steps of the Heun second order sampler (EDM) (Karras et al., 2022). For HT experiments, we use the same EDM sampler and 200 steps across all time horizons to isolate the effect of initialization. A separate denoiser is trained for each time horizon using  $10^5$  samples. For both datasets, we calculate mean  $\pm$  standard deviation (std), over 20 test with  $10^6$  independent samples, of Sliced Wasserstein distance (SWD) using 500 sliced and Max Sliced Wasserstein distance (MaxSWD) using the optimization algorithm described in Section B. In Table 1, we report mean  $\pm$  std of the MaxSWD. Figure 2 shows the quantile estimates (mean  $\pm$  std) for the heavy-tailed case, computed by evaluating on a sample of size  $10^7$  each dimension ( $d = 100$ ) separately and then averaging the results across all dimensions. The results show that the proposed method indeed yield better quality samples across all values of  $\sigma_T$ , in particular on tail reconstruction, enabling either improved sample generation or a reduction in the number of sampling steps. The large standard deviation of MaxSWD in the heavy-tailed setting is intrinsic to heavy-tailed distributions. To better assess improvements in tail generation, we report relative quantile errors in Table 12. SWD results and further experimental details are reported in Section B.1.

**High-Dimensional Image Data.** To demonstrate the scalability and robustness of our approach beyond synthetic

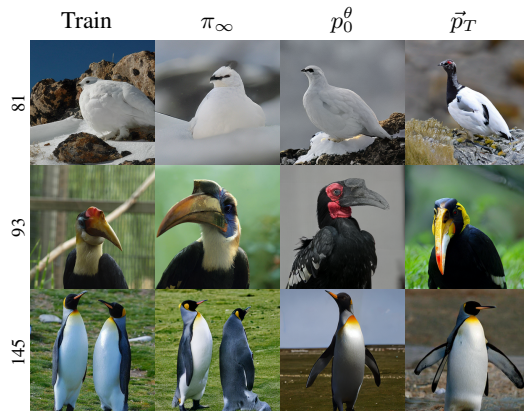


Figure 3. ImageNet<sub>birds</sub> representative nearest neighbor samples per label.

cases, we evaluate its performance on high-dimensional natural image datasets. Specifically, we conduct experiments on FFHQ-64 and a two curated subset of the ImageNet-512 dataset, one consisting of 50 canine classes and the other of 50 birds classes. We refer these two subsets respectively ImageNet<sub>dogs</sub> and ImageNet<sub>birds</sub>. We utilize pre-trained denoiser from Karras et al. (2022) for FFHQ-64 and from Karras et al. (2024) for ImageNet-512. The denoiser for ImageNet-512 is trained on latent representations obtained via Stable VAE (Stability AI, 2025).

**Modeling  $\vec{p}_T$ .** For all datasets, to approximate the intermediate distribution  $\vec{p}_T$ , we use a lightweight version of the Transformer-based Normalizing Flow TarFlow (Zhai et al., 2025), a recent version of Normalizing Flow that shows high performances in image modeling. We trained it on noised data using the strategy of Algorithm 1. In addition, we consider a variant of this training scheme, reported in Algorithm 3, discussed in Section B.2.

**Sampling.** For all datasets, we use the EDM sampler and we consider three initialization strategies. First, we follow the classical procedure starting from a Gaussian prior with time horizon  $\sigma_T = 80$ , using 40 steps for FFHQ-64 and 32 steps for ImageNet-512, as in Karras et al. (2022; 2024). We then compare this baseline with two initializations representing our initialization-aware variants, both starting from a shorter time horizon  $\sigma_T = 7$  and using 20 sampling steps. The two variants use different initialization distributions:  $p_0^\theta$ , corresponding to the normalizing-flow-based initialization trained according to Algorithm 1, and  $\vec{p}_T$ , represented by the noised empirical distribution of training samples. Additional initialization strategies are presented in Section B.2.

**Metrics and Evaluation.** First, we consider Fréchet Inception Distance (FID) (Heusel et al., 2017) to evaluate

Table 3. Results for ImageNet<sub>dogs</sub>

Model	FID	DINO FD	MaxSWD
$\pi_\infty$ (Classic)	10.46	95.30	$3.739 \pm 0.088$
$p_0^\theta$	5.53	70.35	$2.911 \pm 0.073$
$\vec{p}_T$	6.55	68.93	$0.376 \pm 0.665$

Table 4. Results for FFHQ

Model	FID	DINO FD	MaxSWD
$\pi_\infty$ (Classic)	2.53	198.34	$5.380 \pm 0.282$
$p_0^\theta$	3.00	210.86	$3.295 \pm 0.331$
$\vec{p}_T$	2.47	188.70	$0.085 \pm 0.289$

generation quality. FID presents several limitations (Jayasumana et al., 2023; Stein et al., 2023); therefore, we also consider other visual metrics such as Kernel Inception Distance (KID) and Dino Fréchet Distance (DinoFD). We also consider SWD and MaxSWD. For ImageNet-512, SWD and MaxSWD are computed in latent space. While FID, KID, and similar metrics assess realism of generated images, Wasserstein metrics evaluate the fidelity of the underlying probabilistic distribution, which is crucial when realistic appearance is not the main objective. As in (Karras et al., 2022) for the denoiser, we train a single model for  $p_0^\theta$  and perform 3 independent generations. For each run, we compute FID, KID, and DinoFD on  $5 \times 10^4$  generated samples, while SWD are computed on 4 subsets of  $17, 5 \times 10^3$  per generated sample and using  $2 \times 10^4$  slices. MaxSWD follows the same protocol of SWD, but is computed according to Algorithm 2. For all metrics, lower is better. In Table 2, 4 and 3, we report the minimum across the three experiments for FID, KID, and DinoFD, and the aggregated mean  $\pm$  std for SWD and MaxSWD on 12 experiments ( $3 \times 4$ ).  $\pi_\infty$  denotes the classic long horizon generation,  $\vec{p}_T$  the generation initialized with the empirical noised law and  $p_0^\theta$  the generation initialized with the Normalizing Flow. Following standard practice (Karras et al., 2022; 2024), all metrics compare generated data against training data. Using these pre-trained denoisers prevents the use of test data for evaluation. Figure 3 4 present selected training images along with their nearest neighbors across different generated samples, identified using the  $L^2$  distance, to illustrate the diversity of the generated samples.

**Results on Image Datasets.** Our approach considerably improves conditional generation on ImageNet-512, achieving better performance across all metrics while using only 20 steps instead of 32. For FFHQ-64, our method requires half the number of steps and attains significantly better SWD and MaxSWD scores, although image quality metrics are slightly lower than the baseline. Overall, these results



Figure 4. FFHQ representative nearest neighbor samples.

confirm the effectiveness of our initialization strategy in high-dimensional settings, enabling efficient sampling with reduced computational cost, improving conditional generation, and demonstrating the strong potential of initialization-aware in diffusion sampling. Further implementation and results details are provided in Section B.2.

## 5. Discussion and Conclusions

We introduced an initialization-aware strategy for score-based generative models, together with theoretical guarantees that disentangle initialization, discretization, and denoising errors. By starting the reverse process from an intermediate noise level, our approach reduces the effective sampling horizon while preserving generative quality. This offers a principled explanation for several empirical diffusion heuristics and suggests that a shorter generative time horizon can ease the burden on the score model, enabling lighter architectures, faster convergence, and improved stability. At the same time, our work highlights key limitations and directions for future research. In particular, the Lipschitz constant associated with log-concavity cannot be directly inferred from data, so our Lipschitz-based criterion should be viewed as a heuristic rather than a definitive diagnostic, motivating the development of data-driven methods to estimate structural properties of intermediate distributions. Second, our experimental evaluation is restricted to moderate-scale architectures and does not include text-conditioned diffusion models; extending the framework to larger models and more complex conditional settings remains an important and promising direction. A natural extension of this work concerns heavy-tailed distributions. Our results suggest that generating extreme events at an intermediate noise level, followed by refinement, is an effective strategy for modeling heavy-tailed data. Although our analysis and experiments are preliminary and limited to simplified settings, they indicate that intermediate initialization may provide a principled alternative to existing

heavy-tail-specific generative approaches, warranting systematic comparison with VAE- and SGM-based methods (Lafon et al., 2023; Pandey et al., 2025). More broadly, our findings motivate further theoretical and applied work on initialization-aware generative methods, with potential applications to faster flow-matching sampling and improved stability in one- or few-step generative models.

## 6. Discussion and Conclusions

We introduced an initialization-aware strategy for score-based generative models, together with theoretical guarantees that disentangle initialization, discretization, and denoising errors. By starting the reverse process from an intermediate noise level, our approach reduces the effective sampling horizon while preserving generative quality. This offers a principled explanation for several empirical diffusion heuristics and suggests that a shorter generative time horizon can ease the burden on the score model, enabling lighter architectures, faster convergence, and improved stability. At the same time, our work highlights key limitations and directions for future research. In particular, the Lipschitz constant associated with log-concavity cannot be directly inferred from data, so our Lipschitz-based criterion should be viewed as a heuristic rather than a definitive diagnostic, motivating the development of data-driven methods to estimate structural properties of intermediate distributions. Second, our experimental evaluation is restricted to moderate-scale architectures and does not include text-conditioned diffusion models; extending the framework to larger models and more complex conditional settings remains an important and promising direction. A natural extension of this work concerns heavy-tailed distributions. Our results suggest that generating extreme events at an intermediate noise level, followed by refinement, is an effective strategy for modeling heavy-tailed data. Although our analysis and experiments are preliminary and limited to simplified settings, they indicate that intermediate initialization may provide a principled alternative to existing heavy-tail-specific generative approaches, warranting systematic comparison with VAE- and SGM-based methods (Lafon et al., 2023; Pandey et al., 2025). More broadly, our findings motivate further theoretical and applied work on initialization-aware generative methods, with potential applications to faster flow-matching sampling and improved stability in one- or few-step generative models.

## Acknowledgments

This work has been supported by the chair Geolearning, funded by ANDRA, BNP Paribas, CCR and the SCOR Foundation for Science.

## References

- Allouche, M., Girard, S., and Gobet, E. (2022). Ev-gan: Simulation of extreme events with relu neural networks. *Journal of Machine Learning Research*, 23(120):1–39.
- Baldrige, J., Bauer, J., Bhutani, M., Brichtova, N., Bunner, A., Castrejon, L., Chan, K., Chen, Y., Dieleman, S., Du, Y., Eaton-Rosen, Z., Fei, H., de Freitas, N., Gao, Y., Gladchenko, E., Gómez Colmenarejo, S., Guo, M., Haig, A., Hawkins, W., Hu, H., Huang, H., Igwe, T. P., Kaplanis, C., Khodadadeh, S., Kim, Y., Konyushkova, K., Langner, K., Lau, E., Lawton, R., Luo, S., Mokrá, S., Nandwani, H., Onoe, Y., van den Oord, A., Parekh, Z., Pont-Tuset, J., Qi, H., Qian, R., Ramachandran, D., Rane, P., Rashwan, A., Razavi, A., Riachi, R., Srinivasan, H., Srinivasan, S., Strudel, R., Uria, B., Wang, O., Wang, S., Waters, A., Wolff, C., Wright, A., Xiao, Z., Xiong, H., Xu, K., van Zee, M., Zhang, J., Zhang, K., Zhou, W., Zolna, K., and ... (2024). Imagen 3. *arXiv preprint*, arXiv:2408.07009.
- Betker, J., Goh, G., Jing, L., Brooks, T., Wang, J., Li, L., Ouyang, L., Zhuang, J., Lee, J., Guo, Y., Manassra, W., Dhariwal, P., Chu, C., Jiao, Y., and Ramesh, A. (2023). Improving image generation with better captions. Technical report, OpenAI and Microsoft. DALL-E 3 System Card.
- Bingham, N. H., Goldie, C. M., and Teugels, J. L. (1987). *Regular Variation*, volume 27 of *Encyclopedia of Mathematics and its Applications*. Cambridge University Press, Cambridge.
- Bińkowski, M., Sutherland, D. J., Arbel, M., and Gretton, A. (2018). Demystifying MMD GANs. In *International Conference on Learning Representations (ICLR)*.
- Black Forest Labs (2025). Flux.1-dev: 12b-parameter rectified flow transformer for text-to-image generation. <https://huggingface.co/black-forest-labs/FLUX.1-dev>.
- Bortoli, V. D. (2022). Convergence of denoising diffusion models under the manifold hypothesis. *Transactions on Machine Learning Research*. Expert Certification.
- Bruno, S. and Sabanis, S. (2025). Wasserstein convergence of score-based generative models under semiconvexity and discontinuous gradients. *Transactions on Machine Learning Research*. Published 09/2025.
- Chen, N., Zhang, Y., Zen, H., Weiss, R. J., Norouzi, M., and Chan, W. (2021). Wavegrad: Estimating gradients for waveform generation. In *International Conference on Learning Representations*.
- Conforti, G., Durmus, A., and Silveri, M. G. (2025). KL convergence guarantees for score diffusion models under

- minimal data assumptions. *SIAM Journal on Mathematical Analysis*, 7(1):86–109.
- Dalalyan, A. S. (2017). Theoretical guarantees for approximate sampling from smooth and log-concave densities. *Journal of the Royal Statistical Society Series B: Statistical Methodology*, pages 651–676.
- Dhariwal, P. and Nichol, A. Q. (2021). Diffusion models beat GANs on image synthesis. In Beygelzimer, A., Dauphin, Y., Liang, P., and Vaughan, J. W., editors, *Advances in Neural Information Processing Systems*.
- Dinh, L., Sohl-Dickstein, J., and Bengio, S. (2017). Density estimation using real NVP. In *International Conference on Learning Representations*.
- Douc, R., Moulines, E., Priouret, P., and Soulier, P. (2018). *Markov Chains*. Springer Series in Operations Research and Financial Engineering. Springer Nature Switzerland AG, Cham, Switzerland.
- Durmus, A. and Moulines, É. (2017). Nonasymptotic convergence analysis for the unadjusted langevin algorithm. *The Annals of Applied Probability*, 27(3):1551–1587.
- Evans, L. C. (2010). *Partial Differential Equations*, volume 19 of *Graduate Studies in Mathematics*. American Mathematical Society, Providence, RI.
- Feng, R., Yu, C., Deng, W., Hu, P., and Wu, T. (2025). On the guidance of flow matching. In *Forty-second International Conference on Machine Learning*.
- Frey, N. C., Berenber, D., Zadorozhny, K., Kleinhenz, J., Lafrance-Vanasse, J., Hotzel, I., Wu, Y., Ra, S., Bonneau, R., Cho, K., Loukas, A., Gligorijevic, V., and Saremi, S. (2024). Protein discovery with discrete walk-jump sampling. In *The Twelfth International Conference on Learning Representations*.
- Gao, X., Nguyen, H. M., and Zhu, L. (2025). Wasserstein convergence guarantees for a general class of score-based generative models. *Journal of Machine Learning Research*, 26(43):1–54.
- Gao, Y., Huang, J., Jiao, Y., and Zheng, S. (2024). Convergence of continuous normalizing flows for learning probability distributions. *ArXiv*, abs/2404.00551.
- Geng, Z., Deng, M., Bai, X., Kolter, J. Z., and He, K. (2025). Mean flows for one-step generative modeling. In *Advances in Neural Information Processing Systems (NeurIPS)*.
- Hausmann, U. G. and Pardoux, E. (1986). Time reversal of diffusions. *Annals of Probability*, 14(4):1188–1205.
- Heusel, M., Ramsauer, H., Unterthiner, T., Nessler, B., and Hochreiter, S. (2017). Gans trained by a two time-scale update rule converge to a local nash equilibrium. In *Proceedings of the 31st International Conference on Neural Information Processing Systems, NIPS’ 17*, page 6629–6640, Red Hook, NY, USA. Curran Associates Inc.
- Hickling, T. and Prangle, D. (2025). Flexible tails for normalizing flows. In *Forty-second International Conference on Machine Learning*.
- Ho, J., Jain, A., and Abbeel, P. (2020). Denoising diffusion probabilistic models. In *Advances in Neural Information Processing Systems (NeurIPS)*, volume 33, pages 6840–6851. Curran Associates, Inc.
- Issachar, N., Salama, M., Fattal, R., and Benaim, S. (2024). Designing a conditional prior distribution for flow-based generative models.
- Jayasumana, S., Ramalingam, S., Veit, A., Glasner, D., Chakrabarti, A., and Kumar, S. (2023). Rethinking fid: Towards a better evaluation metric for image generation. *2024 IEEE/CVF Conference on Computer Vision and Pattern Recognition (CVPR)*, pages 9307–9315.
- Karras, T., Aittala, M., Aila, T., and Laine, S. (2022). Elucidating the design space of diffusion-based generative models. In Oh, A. H., Agarwal, A., Belgrave, D., and Cho, K., editors, *Advances in Neural Information Processing Systems*.
- Karras, T., Hellsten, J., Lehtinen, J., Laine, S., Aittala, M., and Aila, T. (2024). Analyzing and improving the training dynamics of diffusion models. In *Proceedings of the IEEE/CVF Conference on Computer Vision and Pattern Recognition (CVPR)*, pages 24174–24184.
- Kingma, D. P. and Ba, J. (2014). Adam: A method for stochastic optimization. *CoRR*, abs/1412.6980.
- Kong, Z., Ping, W., Huang, J., Zhao, K., and Catanzaro, B. (2021). Diffwave: A versatile diffusion model for audio synthesis. In *International Conference on Learning Representations*.
- Kornilov, N. M., Mokrov, P., Gasnikov, A., and Korotin, A. (2024). Optimal flow matching: Learning straight trajectories in just one step. In *The Thirty-eighth Annual Conference on Neural Information Processing Systems*.
- Lafon, N., Naveau, P., and Fablet, R. (2023). A vae approach to sample multivariate extremes. *arXiv preprint arXiv:2306.10987*.

- Li, X. L., Thickstun, J., Gulrajani, I., Liang, P., and Hashimoto, T. B. (2022). Diffusion-lm improves controllable text generation. In *Advances in Neural Information Processing Systems (NeurIPS)*, volume 35, pages 4328–4343.
- Lipman, Y., Chen, R. T. Q., Ben-Hamu, H., Nickel, M., and Le, M. (2023). Flow matching for generative modeling. In *The Eleventh International Conference on Learning Representations*.
- Liptser, R. S. and Shiryaev, A. N. (2001). *Statistics of Random Processes I: General Theory*, volume 5 of *Applications of Mathematics*. Springer, second, revised and expanded edition.
- Liu, L., Ren, Y., Lin, Z., and Zhao, Z. (2022). Pseudo numerical methods for diffusion models on manifolds. *ArXiv*, abs/2202.09778.
- McDonald, A., Tan, P.-N., and Luo, L. (2022). Comet flows: Towards generative modeling of multivariate extremes and tail dependence. In *Proceedings of the Thirty-First International Joint Conference on Artificial Intelligence (IJCAI)*, pages 3328–3334. IJCAI Organization.
- Müller-Franzes, G., Niehues, J. M., Khader, F., . . . , and Truhn, D. (2022). Diffusion probabilistic models beat gans on medical images. *arXiv preprint arXiv:2212.07501*.
- Øksendal, B. (2003). *Stochastic Differential Equations: An Introduction with Applications*. Springer-Verlag, Berlin, 6th edition.
- Oquab, M., Darcet, T., Moutakanni, T., Vo, H. V., Szafraniec, M., Khalidov, V., Fernandez, P., HAZIZA, D., Massa, F., El-Nouby, A., Assran, M., Ballas, N., Galuba, W., Howes, R., Huang, P.-Y., Li, S.-W., Misra, I., Rabat, M., Sharma, V., Synnaeve, G., Xu, H., Jegou, H., Mairal, J., Labatut, P., Joulin, A., and Bojanowski, P. (2024). DINOv2: Learning robust visual features without supervision. *Transactions on Machine Learning Research*. Featured Certification.
- Pandey, K., Pathak, J., Xu, Y., Mandt, S., Pritchard, M., Vahdat, A., and Mardani, M. (2025). Heavy-tailed diffusion models. In *The Thirteenth International Conference on Learning Representations*.
- Papamakarios, G., Nalisnick, E., Rezende, D. J., Mohamed, S., and Lakshminarayanan, B. (2021). Normalizing flows for probabilistic modeling and inference. *Journal of Machine Learning Research*, 22(1):1–64.
- Rezende, D. and Mohamed, S. (2015). Variational Inference with Normalizing Flows. In Bach, F. and Blei, D., editors, *Proceedings of the 32nd International Conference on Machine Learning*, volume 37 of *Proceedings of Machine Learning Research*, pages 1530–1538, Lille, France. PMLR.
- Rombach, R., Blattmann, A., Lorenz, D., Esser, P., and Ommer, B. (2022). High-Resolution Image Synthesis with Latent Diffusion Models. In *2022 IEEE/CVF Conference on Computer Vision and Pattern Recognition (CVPR)*, pages 10674–10685, Los Alamitos, CA, USA. IEEE Computer Society.
- Shariatian, D., Simsekli, U., and Durmus, A. O. (2025). Denoising levy probabilistic models. In *The Thirteenth International Conference on Learning Representations*.
- Silveri, M. G. and Ocello, A. (2025). Beyond log-concavity and score regularity: Improved convergence bounds for score-based generative models in w2-distance. In *Forty-second International Conference on Machine Learning*.
- Sohl-Dickstein, J., Weiss, E., Maheswaranathan, N., and Ganguli, S. (2015). Deep unsupervised learning using nonequilibrium thermodynamics. In Bach, F. and Blei, D., editors, *Proceedings of the 32nd International Conference on Machine Learning*, volume 37 of *Proceedings of Machine Learning Research*, pages 2256–2265, Lille, France. PMLR.
- Song, J., Meng, C., and Ermon, S. (2021a). Denoising diffusion implicit models. In *International Conference on Learning Representations*.
- Song, Y., Dhariwal, P., Chen, M., and Sutskever, I. (2023). Consistency models. In *Proceedings of the 40th International Conference on Machine Learning (ICML)*, pages 32211–32252. PMLR.
- Song, Y. and Ermon, S. (2019). Generative modeling by estimating gradients of the data distribution. In *Advances in Neural Information Processing Systems (NeurIPS)*.
- Song, Y., Sohl-Dickstein, J., Kingma, D. P., Kumar, A., Ermon, S., and Poole, B. (2021b). Score-based generative modeling through stochastic differential equations. In *International Conference on Learning Representations*.
- Stability AI (2025). stabilityai/sd-vae-ft-mse. <https://huggingface.co/stabilityai/sd-vae-ft-mse>. Accessed: 2025-12-29.
- Stein, G., Cresswell, J. C., Hosseinzadeh, R., Sui, Y., Ross, B. L., Vилlecroze, V., Liu, Z., Caterini, A. L., Taylor, E., and Loaiza-Ganem, G. (2023). Exposing flaws of generative model evaluation metrics and their unfair treatment of diffusion models. In *Thirty-seventh Conference on Neural Information Processing Systems*.

- Strasman, S., Ocello, A., Boyer, C., Corff, S. L., and Lemaire, V. (2025a). An analysis of the noise schedule for score-based generative models. *Transactions on Machine Learning Research*.
- Strasman, S., Surendran, S., Boyer, C., Le Corff, S., Lemaire, V., and Ocello, A. (2025b). Wasserstein convergence of critically damped langevin diffusions.
- Tang, R. and Yang, Y. (2021). On empirical bayes variational autoencoder: An excess risk bound. In *Proceedings of Thirty Fourth Conference on Learning Theory*, pages 4068–4125. PMLR.
- Tong, A., FATRAS, K., Malkin, N., Huguët, G., Zhang, Y., Rector-Brooks, J., Wolf, G., and Bengio, Y. (2024). Improving and generalizing flow-based generative models with minibatch optimal transport. *Transactions on Machine Learning Research*. Expert Certification.
- Wainwright, M. J. (2019). *High-Dimensional Statistics: A Non-Asymptotic Viewpoint*. Cambridge Series in Statistical and Probabilistic Mathematics. Cambridge University Press.
- Yoon, E., Park, K., Kim, J., and Lim, S. (2022). Score-based generative models with lévy processes. In *NeurIPS 2022 Workshop on Score-Based Methods*.
- Zand, M., Etemad, A., and Greenspan, M. (2024). Diffusion models with deterministic normalizing flow priors. *Transactions on Machine Learning Research*.
- Zhai, S., ZHANG, R., Nakkiran, P., Berthelot, D., Gu, J., Zheng, H., Chen, T., Bautista, M. Á., Jaitly, N., and Susskind, J. M. (2025). Normalizing flows are capable generative models. In *Forty-second International Conference on Machine Learning*.
- Zheng, H., He, P., Chen, W., and Zhou, M. (2023). Truncated diffusion probabilistic models and diffusion-based adversarial auto-encoders. In *The Eleventh International Conference on Learning Representations*.
- Zou, H., Kim, Z. M., and Kang, D. (2023). A survey of diffusion models in natural language processing. *arXiv preprint arXiv:2305.14671*.

## A. Proofs of Results

In this section, we provide the proofs of our main results. The presentation is organized as follows.

- Theorem A.1 in Section A.1 provides a bound on the KL divergence between solutions of SDEs. Variants of this result have been used in prior work (see, e.g., (Conforti et al., 2025; Strasman et al., 2025a)). Since the precise statement and proof are not always presented in full detail in the literature, we provide a complete and self-contained proof tailored to our framework.
- We discuss the existence and regularity of the forward and backward solutions in Section A.2 and establish Lemmas A.2 to A.7 required for the proof of our main result, Theorem 3.1.
- We prove Theorem 3.1 in Section A.3.
- Additional results (Lemma A.8 and Proposition A.9) required for the proof of Theorem A.1 are given in Section A.4.

**Additional notations.** If  $\mu$  and  $\nu$  are two measures on  $(\mathbb{R}^d, \mathcal{B}(\mathbb{R}^d))$ , we write  $\mu \ll \nu$  to state that  $\mu$  is dominated by  $\nu$ . For all random variables  $X$ , we write  $\mu_X$  the law of  $X$  when there is no possible confusion.

### A.1. KL control of SDE solutions

**Theorem A.1.** (*KL control for stochastic differential equation solutions*) Consider the space of continuous functions  $\mathcal{C}_T = \mathcal{C}([0, T], \mathbb{R}^d)$ , endowed with the  $\sigma$ -algebra induced by the uniform convergence topology on the full product space  $\prod_{t \in [0, T]} \mathbb{R}^d$ . We consider the following SDE

$$dX_t = A_t(X) dt + b_t dB_t, \quad (17)$$

and

$$dY_t = a_t(Y) dt + b_t dB_t, \quad (18)$$

where  $A_t(X) = A(t, X_{[0, t]})$ ,  $a_t(Y) = a(t, Y_{[0, t]})$  and  $b_t$  is a strictly positive noise schedule. We suppose the existence of strong solutions  $X$  and  $Y$  to respectively Equation (17) and Equation (18) initialized with  $X_0, Y_0$  on  $(\mathbb{R}^d, \mathcal{B}(\mathbb{R}^d))$  such that  $\mu_{X_0} \ll \mu_{Y_0}$ . For all  $x \in \mathbb{R}^d$ , we also suppose the existence of  $X^x$  and  $Y^x$ , strong solutions to Equation (17) and Equation (18) initialized at  $x$ . Assume that for  $\mu_{X_0}$ -almost every  $x$

$$\mathbb{P} \left( \int_0^T \frac{1}{b_s^2} (\|A_t(X^x)\|^2 + \|a_t(X^x)\|^2) ds < \infty \right) = 1. \quad (19)$$

Then,  $\mu_X \ll \mu_Y$  and

$$D_{\text{KL}}(\mu_X || \mu_Y) = D_{\text{KL}}(\mu_{X_0} || \mu_{Y_0}) + \mathbb{E} \left[ \frac{1}{2} \int_0^T \frac{1}{b_s^2} \|A_t(X) - a_t(X)\|^2 ds \right].$$

*Proof.* Using that the condition  $b_t > 0$  ensures that  $(A_t(X) - a_t(X))/b_t$  is well defined, that there exist strong solutions to (17) and (18) and by (19), for  $\mu_{X_0}$ -almost every  $x$ , we can apply Liptser and Shiryaev (2001, Theorem 7.20) with  $\xi = X^x$  and  $\eta = Y^x$ . Therefore,  $\mu_{X^x} \ll \mu_{Y^x}$  and

$$\frac{d\mu_{X^x}}{d\mu_{Y^x}}(X^x) = \exp \left\{ \int_0^T \frac{A_t(X^x) - a_t(X^x)}{b_t^2} dX_t^x - \int_0^T \frac{(A_t(X^x) - a_t(X^x))^T \cdot (A_t(X^x) + a_t(X^x))}{2b_t^2} dt \right\}.$$

The conditional law of  $X$  given  $X_0 = x$ , written  $\mu_{X|X_0}(\cdot | x)$ , coincides with  $\mu_{X^x}$ , and similarly  $\mu_{Y|Y_0}(\cdot | x)$  coincides with  $\mu_{Y^x}$ . Hence, for  $\mu_{X_0}$ -almost every  $x$ , we have

$$\mu_{Y|Y_0}(\cdot | x) \ll \mu_{X|X_0}(\cdot | x).$$

From Proposition A.9 applied to  $E = \mathcal{C}_T$ ,  $F = \mathbb{R}^d$  and  $T$  the projection that associates to the solution its initialization we can state that  $\mu_X \ll \mu_Y$  and

$$D_{\text{KL}}(\mu_X || \mu_Y) = D_{\text{KL}}(\mu_{X_0} || \mu_{Y_0}) + \mathbb{E} \left[ \log \left( \frac{d\mu_{X|X_0}}{d\mu_{Y|Y_0}}(X | X_0) \right) \right].$$

In order to conclude the proof we have to show that

$$\mathbb{E} \left[ \log \left( \frac{d\mu_{X|X_0}}{d\mu_{Y|Y_0}}(X | X_0) \right) \right] = \mathbb{E} \left[ \frac{1}{2} \int_0^T \frac{1}{b_s^2} \|A_s(X) - a_s(X)\|^2 ds \right].$$

We have

$$\begin{aligned} \mathbb{E} \left[ \log \left( \frac{d\mu_{X|X_0}}{d\mu_{Y|Y_0}}(X | X_0) \right) \right] &= \int_{\mathcal{C}_T \times \mathbb{R}^d} \log \left( \frac{d\mu_{X|X_0}}{d\mu_{Y|Y_0}}(x | x_0) \right) d\mu_{X, X_0}(x, x_0) \\ &= \int_{\mathbb{R}^d} \int_{\mathcal{C}_T} \log \left( \frac{d\mu_{X|X_0}}{d\mu_{Y|Y_0}}(x | x_0) \right) d\mu_{X|X_0}(x | x_0) d\mu_{X_0}(x_0) \\ &= \int_{\mathbb{R}^d} \mathbb{E} \left[ \log \frac{d\mu_{X^{x_0}}}{d\mu_{Y^{x_0}}}(X^{x_0}) \right] d\mu_{X_0}(x_0). \end{aligned} \quad (20)$$

We can also write

$$\begin{aligned} \mathbb{E} \left[ \log \frac{d\mu_{X^{x_0}}}{d\mu_{Y^{x_0}}}(X^{x_0}) \right] &= \mathbb{E} \left[ \int_0^T \frac{(A_t(X^x) - a_t(X^x))^T A_t(X^x)}{b_t^2} dt + \int_0^T \frac{A_t(X^x) - a_t(X^x)}{b_t} dB_t \right. \\ &\quad \left. - \int_0^T \frac{(A_t(X^x) - a_t(X^x))^T (A_t(X^x) + a_t(X^x))}{2b_t^2} dt \right] \\ &= \mathbb{E} \left[ \int_0^T \frac{\|A_t(X^x) - a_t(X^x)\|^2}{2b_t^2} dt \right]. \end{aligned} \quad (21)$$

So, we have

$$\begin{aligned} \mathbb{E} \left[ \log \left( \frac{d\mu_{X|X_0}}{d\mu_{Y|Y_0}}(X | X_0) \right) \right] &= \int_{\mathbb{R}^d} \mathbb{E} \left[ \int_0^T \frac{\|A_t(X^x) - a_t(X^x)\|^2}{2b_t^2} dt \right] d\mu_{X_0}(x_0) \\ &= \int_{\mathbb{R}^d} \int_{\mathcal{C}_T} \int_0^T \frac{\|A_t(x) - a_t(x)\|^2}{2b_t^2} dt d\mu_{X^{x_0}}(x) d\mu_{X_0}(x_0) \\ &= \int_{\mathbb{R}^d} \int_{\mathcal{C}_T} \int_0^T \frac{\|A_t(x) - a_t(x)\|^2}{2b_t^2} dt d\mu_{X|X_0}(x | x_0) d\mu_{X_0}(x_0) \\ &= \int_{\mathcal{C}_T \times \mathbb{R}^d} \int_0^T \frac{\|A_t(x) - a_t(x)\|^2}{2b_t^2} dt d\mu_{X, X_0}(x, x_0) \\ &= \int_{\mathcal{C}_T} \int_0^T \frac{\|A_t(x) - a_t(x)\|^2}{2b_t^2} dt d\mu_X(x) \\ &= \mathbb{E} \left[ \frac{1}{2} \int_0^T \frac{1}{b_s^2} \|A_s(X) - a_s(X)\|^2 ds \right], \end{aligned} \quad (22)$$

which concludes the proof.  $\square$

## A.2. Lemmas required for Theorem 3.1

Following Theorem 5.2.1 in (Øksendal, 2003), it is easy to show that if  $\vec{X}_0 \in L^2(\Omega, \mathcal{F}, \mathbb{P})$  and if  $t \mapsto \alpha_t$ , and  $t \mapsto g_t$  are bounded, the existence and uniqueness of a solution to Equation (1) are guaranteed. Concerning the regularity of the forward

density  $\vec{p}_t$  of Equation (1), for our work, we need it to be in  $C^1((0, T])$  for the time variable and in  $C^2(\mathbb{R}^d)$  for the state variable. Instead of showing the result in the general case, we show it in Lemma A.2 just for the Variance Exploding case of Equation (2).

The proof for the VE case is sufficient because the density of the solution of Equation (1) and Equation (2) can be reciprocally obtained by a  $C^\infty([0, T] \times \mathbb{R}^d)$  transformation (for details see (Karras et al., 2022)).

**Lemma A.2.** *Consider the forward equation (2). If  $\vec{X}_0 \in L^2(\Omega, \mathcal{F}, \mathbb{P})$ , for all  $x \in \mathbb{R}^d$ ,  $t \mapsto \vec{p}_t(x)$  is in  $C^\infty((0, T])$  and for all  $t \in (0, T]$ ,  $x \mapsto \vec{p}_t(x)$  is in  $C^\infty(\mathbb{R}^d)$  and therefore  $(t, x) \mapsto \vec{p}_t(x)$  is in  $C^\infty((0, T] \times \mathbb{R}^d)$ .*

*Proof.* We show that for all  $t \in (0, T]$ ,  $x \mapsto \vec{p}_t(x)$  is in  $C^2(\mathbb{R}^d)$  and that for all  $x \in \mathbb{R}^d$ ,  $t \mapsto \vec{p}_t(x)$  is in  $C^1((0, T])$ . The proof follows the same step for higher regularity orders. In the VE setting, the density can be written as

$$\vec{p}_t(x) = \int_{\mathbb{R}^d} \vec{p}_0(y) q_t(y | x) dy ,$$

where  $q_t(\cdot | x)$  is the density of a Gaussian centered at  $x$  with variance  $\sigma_t^2 I_d$ . To show derivability at  $t_0 > 0$  for a fixed  $x$ , consider any interval  $[t_1, t_2] \subset (0, T]$ . In order to apply the dominated convergence theorem, it suffices to differentiate the integrand and bound the  $t$ -dependent terms by their maximum on this interval. Recalling that  $z \mapsto z^k e^{-z^2/2}$  is bounded for all  $k \in \mathbb{N}$ , the desired regularity follows immediately. To show double differentiability in  $x \in \mathbb{R}^d$  for a fixed  $t$ , it is again enough to differentiate the integrand and note that  $z \mapsto z^k e^{-z^2/2}$  is bounded for all  $k \in \mathbb{N}$ . From the differentiability to the continuity of the derivative, the implication is immediate: the functions appearing in the integrand that defines the density and its derivatives belong to  $C^\infty((0, T] \times \mathbb{R}^d)$ .  $\square$

**Lemma A.3.** *If  $\vec{X}_0 \in L^2(\Omega, \mathcal{F}, \mathbb{P})$ , for all  $\delta > 0$ , there exists a strong solution to the following equation on  $[0, T - \delta]$*

$$d\vec{X}_t = \left\{ \vec{\alpha}_t \vec{X}_t + \vec{g}_t^2 \nabla \log \vec{p}_{T-t}(\vec{X}_t) \right\} dt + \vec{g}_t d\vec{B}_t , \quad (23)$$

such that for all  $t \in [0, T - \delta]$   $\vec{X}_t = \vec{X}_{T-t}$ .

*Proof.* Following Haussmann and Pardoux (1986), Equation (2) satisfies the standard conditions for the existence of a forward solution thanks to Hypothesis 1. Moreover, its forward solution admits a density  $\vec{p}_t(x)$  for all  $0 < t \leq T$ . To show the existence of the backward equation, it suffices to prove that, for any  $t_0 > 0$  and any bounded open set  $A \subset \mathbb{R}^d$ ,  $\int_{t_0}^T \int_A \vec{p}_t(x)^2 + g_t^2 \|\nabla \vec{p}_t(x)\|^2 dx dt < +\infty$ . As in Lemma A.2,  $\vec{p}_t(x)$  and  $\nabla \vec{p}_t(x)$  are bounded, and  $g_t$  is bounded on any compact interval  $[t_0, T]$  because it is continuous. Hence, the integral is finite, and the conclusion follows.  $\square$

The regularity result is necessary to obtain this generalized version of the Fokker-Planck equation, necessary for the analysis of the dynamics of the score.

**Lemma A.4** (Fokker–Planck Equation). *If  $\vec{X}_0 \in L^2(\Omega, \mathcal{F}, \mathbb{P})$ , we have, for all  $t \in (0, T]$  and  $x \in \mathbb{R}^d$ ,*

$$\partial_t \vec{p}_t(x) = \alpha_t \operatorname{div}(x \vec{p}_t(x)) + \frac{g_t}{2} \Delta \vec{p}_t(x) .$$

*Proof.* We report Fokker Planck equation proof for completeness. Consider the forward equation (1). We know that the density of the solution is sufficiently regular and consider a test function  $\phi : \mathbb{R}^d \rightarrow \mathbb{R}$ . By Ito's Formula,

$$\mathbb{E}[\phi(\vec{X}_t)] - \mathbb{E}[\phi(\vec{X}_0)] = \int_0^t \left( \mathbb{E}[-\alpha_t \nabla \phi(\vec{X}_t) \cdot \vec{X}_t] + \mathbb{E} \left[ \frac{g_t^2}{2} \Delta \phi(\vec{X}_t) \right] \right) dt . \quad (24)$$

Therefore,

$$\frac{d}{dt} \mathbb{E}[\phi(\vec{X}_t)] = \mathbb{E}[-\alpha_t \nabla \phi(\vec{X}_t) \cdot \vec{X}_t] + \mathbb{E} \left[ \frac{g_t^2}{2} \Delta \phi(\vec{X}_t) \right] . \quad (25)$$

Using the dominated convergence theorem yields

$$\int_{\mathbb{R}^d} \phi(x) \frac{\partial}{\partial t} \vec{p}_t(x) dx = -\alpha_t \int_{\mathbb{R}^d} \nabla \phi(x) \cdot x \vec{p}_t(x) dx + \frac{g_t^2}{2} \int_{\mathbb{R}^d} \Delta \phi(x) \vec{p}_t(x) dx . \quad (26)$$

Thanks to regularity of  $\vec{p}_t$  and using integration by parts for the first term on the right hand side and Green's Formula for the second we can write

$$\int_{\mathbb{R}^d} \phi(x) \frac{\partial}{\partial t} \vec{p}_t(x) dx = \alpha_t \int_{\mathbb{R}^d} \phi(x) \cdot \operatorname{div}(x \vec{p}_t(x)) dx + \frac{g_t^2}{2} \int_{\mathbb{R}^d} \phi(x) \Delta \vec{p}_t(x) dx . \quad (27)$$

The last equality is true for any test function which concludes the proof.  $\square$

Consider a sufficiently regular function  $\rho : \mathbb{R}^d \rightarrow \mathbb{R}^+ / \{0\}$  and define for all  $x \in \mathbb{R}^d$ ,

$$\tilde{p}_t(x) = \frac{\vec{p}_t(x)}{\rho(x)} . \quad (28)$$

**Lemma A.5.** *If  $\vec{X}_0 \in L^2(\Omega, \mathcal{F}, \mathbb{P})$ , for all  $x \in \mathbb{R}^d$  and all  $0 \leq t < T$ ,*

$$\begin{aligned} \partial_t \tilde{p}_{T-t}(x) \rho(x) + \bar{\alpha}_t \left[ \rho(x) \nabla \tilde{p}_{T-t}(x) \cdot x + \tilde{p}_{T-t}(x) \nabla \rho(x) \cdot x + d \tilde{p}_{T-t}(x) \rho(x) \right] \\ + \frac{\bar{g}_t^2}{2} \left[ \rho(x) \Delta \tilde{p}_{T-t}(x) + \tilde{p}_{T-t}(x) \Delta \rho(x) + 2 \nabla \tilde{p}_{T-t}(x) \cdot \nabla \rho(x) \right] = 0 . \end{aligned}$$

*Proof.* From Lemma A.4 we know the form of Fokker Planck equation for the density  $\vec{p}_t$  solution to (1). We also know that for all  $x \in \mathbb{R}^d$ ,  $\vec{p}_t(x) = \tilde{p}_t(x) \rho(x)$ . By simply injecting this last formula in the Fokker Planck equation, we get the result.  $\square$

**Lemma A.6.** *Let  $Y_t = \nabla \log \tilde{p}_{T-t}(\vec{X}_t)$ , where  $\tilde{p}_t$  is defined in (28) and  $\vec{X}_t$  is solution to Equation (23). Then, under the hypotheses of Lemma A.5, for all  $\delta > 0$ , on the interval  $[0, T - \delta]$ , the score satisfies the SDE:*

$$\begin{aligned} dY_t = -\bar{\alpha}_t \left[ Y_t + \nabla^2 \log \rho(\vec{X}_t) \vec{X}_t + \nabla \log \rho(\vec{X}_t) \right] dt \\ - \bar{g}_t^2 \left[ \nabla^2 \log \rho(\vec{X}_t) Y_t + \frac{1}{2} \nabla \left( \frac{\Delta \rho(\vec{X}_t)}{\rho(\vec{X}_t)} \right) \right] dt + \bar{g}_t Z_t dB_t , \quad (29) \end{aligned}$$

where  $Z_t = \nabla Y_t$ , which is a.s. well defined.

*Proof.* We can reformulate the result of Lemma A.5 as:

$$\begin{aligned} \partial_t \log \tilde{p}_{T-t}(x) \rho(x) + \bar{\alpha}_t \left[ \rho(x) \nabla \log \tilde{p}_{T-t}(x) \cdot x + \nabla \rho(x) \cdot x + d \rho(x) \right] \\ + \frac{\bar{g}_t^2}{2} \left[ \rho(x) \frac{\Delta \tilde{p}_{T-t}(x)}{\tilde{p}_{T-t}(x)} + \Delta \rho(x) + 2 \nabla \log \tilde{p}_{T-t}(x) \cdot \nabla \rho(x) \right] = 0 . \end{aligned}$$

Using the general property

$$\frac{\Delta f(x)}{f(x)} = \Delta f(x) + \|\nabla f(x)\|^2 ,$$

we can write

$$\begin{aligned} \partial_t \log \tilde{p}_{T-t}(x) \rho(x) + \bar{\alpha}_t \left[ \rho(x) \nabla \log \tilde{p}_{T-t}(x) \cdot x + \nabla \rho(x) \cdot x + d \rho(x) \right] \\ + \frac{\bar{g}_t^2}{2} \left[ \rho(x) [\Delta \log \tilde{p}_{T-t}(x) + \|\nabla \log \tilde{p}_{T-t}(x)\|^2] + \Delta \rho(x) + 2 \nabla \log \tilde{p}_{T-t}(x) \cdot \nabla \rho(x) \right] = 0 , \end{aligned}$$

and so

$$\begin{aligned} \partial_t \log \tilde{p}_{T-t}(x) + \frac{\bar{g}_t^2}{2} \left[ \Delta \log \tilde{p}_{T-t}(x) + \|\nabla \log \tilde{p}_{T-t}(x)\|^2 \right] \\ = -\frac{\bar{g}_t^2}{2} \left[ \frac{\Delta \rho(x)}{\rho(x)} + 2 \nabla \log \tilde{p}_{T-t}(x) \cdot \nabla \log \rho(x) \right] - \bar{\alpha}_t \left[ \nabla \log \tilde{p}_{T-t}(x) \cdot x + \nabla \log \rho(x) \cdot x + d \right] . \end{aligned}$$

Using  $\overleftarrow{X}_t$  in the last equation and defining  $\Phi_t = \log \vec{p}_{T-t}(\overleftarrow{X}_t)$  we finally write

$$\partial_t \Phi_t + \frac{\bar{g}_t^2}{2} (\|\nabla \Phi_t\|^2 + \Delta \Phi_t) = -\bar{\alpha}_t \left[ \nabla \Phi_t \cdot \overleftarrow{X}_t + \nabla \log \rho(\overleftarrow{X}_t) \cdot \overleftarrow{X}_t + d \right] - \frac{\bar{g}_t^2}{2} \left[ \frac{\Delta \rho}{\rho}(\overleftarrow{X}_t) + 2 \nabla \log \rho \cdot \nabla \Phi_t \right]. \quad (30)$$

The score function  $Y_t = \nabla \log \vec{p}_{T-t}(\overleftarrow{X}_t)$  is well defined and we can apply Ito's Formula to Equation (23) and noting that  $Y_t = \nabla \Phi_t$  yields

$$\begin{aligned} dY_t &= \left( \partial_t \nabla \Phi_t + \nabla^2 \Phi_t \left[ \bar{\alpha}_t \overleftarrow{X}_t + \bar{g}_t^2 \left( \nabla \log \rho(\overleftarrow{X}_t) + \nabla \Phi_t \right) \right] + \frac{\bar{g}_t^2}{2} \Delta \nabla \Phi_t \right) dt + \bar{g}_t \nabla^2 \Phi_t dB_t \\ &= \left( \partial_t \nabla \Phi_t + \bar{g}_t^2 \nabla^2 \Phi_t \nabla \Phi_t + \frac{\bar{g}_t^2}{2} \Delta \nabla \Phi_t + \bar{\alpha}_t \nabla^2 \Phi_t \overleftarrow{X}_t + \bar{g}_t^2 \nabla^2 \Phi_t \nabla \log \rho(\overleftarrow{X}_t) \right) dt + \bar{g}_t \nabla^2 \Phi_t dB_t \\ &= \nabla \left\{ \partial_t \Phi_t + \frac{\bar{g}_t^2}{2} \|\nabla \Phi_t\|^2 + \frac{\bar{g}_t^2}{2} \Delta \Phi_t \right\} dt + \left( \bar{\alpha}_t \nabla^2 \Phi_t \overleftarrow{X}_t + \bar{g}_t^2 \nabla^2 \Phi_t \nabla \log \rho(\overleftarrow{X}_t) \right) dt + \bar{g}_t \nabla^2 \Phi_t dB_t. \end{aligned}$$

Combining Equation (30) and the last equation concludes the proof.  $\square$

We established a general result for analyzing the dynamics of the score function in the general setting of Equation (1). Replacing  $\alpha_t, g_t$  with appropriate schedulers and choosing  $\rho = \phi$  where  $\phi$  denotes the density of the Gaussian distribution  $\mathcal{N}(0, I_d)$ , we recover [Strasman et al. \(2025a, Lemma B.7\)](#) and [Conforti et al. \(2025, Proposition 2\)](#). Our interest lies in studying the score function of the variance exploding setting: Equation (2) and Equation (3). To obtain VE equation from Equation (1) it is sufficient to choose  $\alpha_t = 0$  and to obtain the result we need for Equation (13) we find that  $\rho(x) = 1$  is the right choice. Thanks to [Lemma A.6](#) using  $\rho(x) = 1$  we have that for all  $\delta > 0$ , on the interval  $[0, T - \delta]$ ,  $Y_t = \nabla \log \vec{p}_{T-t}(\overleftarrow{X}_t)$  satisfies:

$$dY_t = \bar{g}_t Z_t d\tilde{B}_t.$$

By applying Itô's formula like in ([Conforti et al., 2025](#)), we also obtain:

$$d\|Y_t\|^2 = \bar{g}_t^2 \|Z_t\|_{Fr}^2 dt + 2\bar{g}_t^2 Y_t^\top Z_t d\tilde{B}_t.$$

We show here that the norm of the score function  $\nabla \log \vec{p}_{T-t}(\overleftarrow{X}_t)$  is a martingale.

**Lemma A.7.** *If  $\mu_*$  has a finite moment of order 2, then*

$$\mathbb{E} \left[ \int_0^{T-\delta} \|Y_s^\top Z_s\|^2 ds \right] < \infty.$$

*Proof.* Note that for all vector  $x$  and matrix  $A$ ,  $\|Ax\| \leq \|A\|_{Fr} \|x\|$ . Therefore,

$$\|Y_s^\top Z_s\|^2 \leq \|Y_s^\top\|^2 \|Z_s\|_{Fr}^2 \leq \frac{1}{2} (\|Y_s^\top\|^4 + \|Z_s\|_{Fr}^4).$$

We first show that  $\mathbb{E}[\int_0^{T-\delta} \|Y_s^\top\|^4 ds] < \infty$ . We know that

$$\vec{p}_t(x) = \int_{\mathbb{R}^d} \vec{p}_0(y) q_t(x | y) dy,$$

where the transition density is given by

$$q_t(x | y) = \frac{1}{(2\pi\sigma_t^2)^{d/2}} \exp \left\{ -\frac{\|x - y\|^2}{2\sigma_t^2} \right\},$$

with  $\sigma_t^2 = \int_0^t g_s^2 ds$ . Therefore,

$$\begin{aligned} \nabla \log \vec{p}_t(x) &= \frac{\nabla \vec{p}_t(x)}{\vec{p}_t(x)} \\ &= \frac{1}{\vec{p}_t(x)} \int \nabla q_t(x | y) \vec{p}_0(y) dy \\ &= -\frac{1}{\sigma_t^2 \vec{p}_t(x)} \int (x - y) \vec{p}_0(y) q_t(x | y) dy, \end{aligned} \quad (31)$$

and

$$\mathbb{E}[\|\nabla \log \vec{p}(\vec{X}_{T-s})\|^4] = \sigma_t^{-8} \mathbb{E}[\|\mathbb{E}[\vec{X}_{T-s} - X_0 | \vec{X}_{T-s}]\|^4] \leq \sigma_t^{-8} \mathbb{E}[\|\vec{X}_{T-s} - X_0\|^4] < \infty.$$

Then, we show that  $\mathbb{E}[\int_0^{T-\delta} \|Z_s\|_{\mathbb{F}^d}^4 ds] < \infty$ . Write

$$\nabla^2 \vec{p}_t(x) = \frac{1}{\sigma_t^4} \int_{\mathbb{R}^d} [(x-y)(x-y)^\top - \sigma_t^2 \mathbf{I}_d] \vec{p}_0(y) q_t(x|y) dy,$$

and

$$\nabla^2 \log \vec{p}_t(x) = \frac{\nabla^2 \vec{p}_t(x)}{\vec{p}_t(x)} - \nabla \log \vec{p}_t(x) \nabla \log \vec{p}_t(x)^\top.$$

So we have

$$\begin{aligned} \nabla^2 \log \vec{p}_t(x) &= \frac{1}{\sigma_t^4 \vec{p}_t(x)} \int_{\mathbb{R}^d} [(x-y)(x-y)^\top - \sigma_t^2 \mathbf{I}_d] \vec{p}_0(y) q_t(x|y) dy \\ &\quad - \frac{1}{\sigma_t^4 \vec{p}_t(x)^2} \left( \int_{\mathbb{R}^d} (x-y) \vec{p}_0(y) q_t(x|y) dy \right) \left( \int_{\mathbb{R}^d} (x-y) \vec{p}_0(y) q_t(x|y) dy \right)^\top. \end{aligned}$$

Finally,

$$\begin{aligned} \nabla^2 \log \vec{p}_t(\vec{X}_{T-s}) &= \frac{1}{\sigma_{T-s}^4} \mathbb{E} \left[ (\vec{X}_{T-s} - X_0)(\vec{X}_{T-s} - X_0)^\top - \sigma_{T-s}^2 \mathbf{I}_d \mid \vec{X}_{T-s} \right] \\ &\quad - \frac{1}{\sigma_{T-s}^4} \mathbb{E} \left[ X_0 - \vec{X}_{T-s} \mid \vec{X}_{T-s} \right] \mathbb{E} \left[ X_0 - \vec{X}_{T-s} \mid \vec{X}_{T-s} \right]^\top. \end{aligned}$$

This yields

$$\begin{aligned} \mathbb{E} \left[ \left\| \nabla^2 \log \vec{p}_t(\vec{X}_{T-s}) \right\|^4 \right] &= \mathbb{E} \left[ \left\| \frac{1}{\sigma_{T-s}^4} \mathbb{E} \left[ (\vec{X}_{T-s} - X_0)(\vec{X}_{T-s} - X_0)^\top - \sigma_{T-s}^2 \mathbf{I}_d \mid \vec{X}_{T-s} \right] \right. \right. \\ &\quad \left. \left. - \frac{1}{\sigma_{T-s}^4} \mathbb{E} \left[ X_0 - \vec{X}_{T-s} \mid \vec{X}_{T-s} \right] \mathbb{E} \left[ X_0 - \vec{X}_{T-s} \mid \vec{X}_{T-s} \right]^\top \right\|^4 \right] \\ &\leq \frac{C_1}{\sigma_{T-s}^{16}} \mathbb{E} \left[ \left\| (\vec{X}_{T-s} - X_0)(\vec{X}_{T-s} - X_0)^\top - \sigma_{T-s}^2 \mathbf{I}_d \right\|^4 \right] \\ &\quad + \frac{C_2}{\sigma_{T-s}^{16}} \mathbb{E} \left[ \left\| (X_0 - \vec{X}_{T-s})(X_0 - \vec{X}_{T-s})^\top \right\|^4 \right], \end{aligned}$$

where  $C_1, C_2$  are positive constants. The proof is concluded by noting that  $\vec{X}_{T-s} - X_0$  is has a Gaussian distribution.  $\square$

### A.3. Proof of Theorem 3.1

We can finally prove Theorem 3.1 in the first form using Equations (9) to (11) and in the form of Equation (13). We consider  $\delta \geq 0$ . The existence of the strong solutions  $\{\check{X}_t\}_{t \in [0, T-\delta]}$ ,  $\{\check{X}_t^x\}_{t \in [0, T-\delta]}$  is guaranteed by Lemma A.3. Writing  $X_t^{\theta, x}$  the solution of the discretized backward with deterministic initialization  $x$ , the strong existence of  $\{X_t^\theta\}_{t \in [0, T-\delta]}$  and  $Y^x = \{X_t^{\theta, x}\}_{t \in [0, T-\delta]}$  follows from the explicit form of the solution. Thanks to Hypothesis H1 we know that  $p_0^\theta > 0$   $\lambda_{\mathbb{R}^d}$ -almost surely and therefore  $\check{X}_0 \ll X_0^\theta$ . Considering also Hypothesis H2, we can therefore apply theorem Theorem A.1 with

- $X = \{\check{X}_t\}_{t \in [0, T-\delta]}$ ,  $Y = \{X_t^\theta\}_{t \in [0, T-\delta]}$ .
- $X^x = \{\check{X}_t^x\}_{t \in [0, T-\delta]}$ ,  $Y^x = \{X_t^{\theta, x}\}_{t \in [0, T-\delta]}$ .
- $X_0 = \check{X}_0$ ,  $Y_0 \sim p_0^\theta$ .

The KL bound we obtain is the following :

$$\begin{aligned} D_{\text{KL}}(\vec{p}_\delta \| p_{T-\delta}^\theta) &\leq D_{\text{KL}}(\vec{p}_T \| p_0^\theta) + \\ &= \frac{1}{2} \int_0^{T-\delta} \frac{1}{\bar{g}_t^2} \mathbb{E} \left[ \left\| \bar{g}_t^2 \nabla \log \vec{p}_{T-t}(\bar{X}_t) - \sum_{k=0}^{N-1} \bar{g}_t^2 s_\theta(T-t_k, \bar{X}_{t_k}) \mathbb{1}_{[t_k, t_{k+1})}(t) \right\|^2 \right] dt, \end{aligned} \quad (32)$$

Using the square triangular inequality and extracting  $\bar{g}_t$ , we get that

$$\begin{aligned} D_{\text{KL}}(\vec{p}_\delta \| p_{T-\delta}^\theta) &\leq D_{\text{KL}}(\vec{p}_T \| p_0^\theta) \\ &+ \sum_{k=0}^{N-1} \int_{t_k}^{t_{k+1}} \bar{g}_t^2 dt \mathbb{E} \left[ \left\| \nabla \log \vec{p}_{T-t_k}(\bar{X}_{t_k}) - s_\theta(T-t_k, \bar{X}_{t_k}) \right\|^2 \right] \\ &+ \sum_{k=0}^{N-1} \int_{t_k}^{t_{k+1}} \bar{g}_t^2 \mathbb{E} \left[ \left\| \nabla \log \vec{p}_{T-t_k}(\bar{X}_{t_k}) - \nabla \log \vec{p}_{T-t}(\bar{X}_t) \right\|^2 \right] dt, \end{aligned} \quad (33)$$

We obtained Theorem 3.1 with terms Equations (9) to (11). To obtain Equation (12), using the definition of  $Y_t$  write

$$\sum_{k=0}^{N-1} \int_{t_k}^{t_{k+1}} \bar{g}_t^2 \mathbb{E} \left[ \left\| \nabla \log \vec{p}_{T-t_k}(\bar{X}_{t_k}) - \nabla \log \vec{p}_{T-t}(\bar{X}_t) \right\|^2 \right] dt = \sum_{k=0}^{N-1} \int_{t_k}^{t_{k+1}} \bar{g}_t^2 \mathbb{E} \left[ \|Y_{t_k} - Y_t\|^2 \right] dt.$$

The expected value inside the integral can be written

$$\mathbb{E} \left[ \left\| \int_{t_k}^t \bar{g}_s Z_s dB_s \right\|^2 \right] = \mathbb{E} \left[ \int_{t_k}^t \|\bar{g}_s Z_s\|_{\mathbb{F}_T}^2 ds \right].$$

Then, note that

$$\sum_{k=0}^{N-1} \int_{t_k}^{t_{k+1}} \bar{g}_t^2 \mathbb{E} \left[ \int_{t_k}^t \|\bar{g}_s Z_s\|_{\mathbb{F}_T}^2 ds \right] dt \leq \sum_{k=0}^{N-1} \int_{t_k}^{t_{k+1}} \bar{g}_t^2 \mathbb{E} \left[ \int_{t_k}^{t_{k+1}} \|\bar{g}_s Z_s\|_{\mathbb{F}_T}^2 ds \right] dt.$$

Thanks to Lemma A.6 and Lemma A.7 we know that the norm of the score evolves as an SDE and defines the diffusion part defines a martingal, so that the second term of the last inequality can be upper bounded as follows

$$\sum_{k=0}^{N-1} (\|Y_{t_{k+1}}\|^2 - \|Y_{t_k}\|^2) \int_{t_k}^{t_{k+1}} \bar{g}_t^2 dt \leq \max_{k=0, \dots, N-1} \left\{ \int_{t_k}^{t_{k+1}} \bar{g}_t^2 dt \right\} \sum_{k=0}^{N-1} (\|Y_{t_{k+1}}\|^2 - \|Y_{t_k}\|^2).$$

We note the telescopic sum and we conclude

$$E_{\text{disc}} \leq \max_{k=0, \dots, N-1} \left\{ \int_{t_k}^{t_{k+1}} \bar{g}_t^2 dt \right\} \cdot \left( \mathcal{I}(\vec{p}_\delta) - \mathcal{I}(\vec{p}_T) \right),$$

where  $E_{\text{disc}}$  is defined in Theorem 3.1.

#### A.4. Results for the proof of Theorem A.1

**Lemma A.8** (Conditional absolute continuity). *Let  $(E, \mathcal{E})$  and  $(F, \mathcal{F})$  be Polish spaces. Let  $X, Y : (\Omega, \mathcal{A}, \mathbb{P}) \rightarrow (E, \mathcal{E})$  be random variables and let  $T : (E, \mathcal{E}) \rightarrow (F, \mathcal{F})$  be a measurable map. Denote by  $\mu_X, \mu_Y$  the laws of  $X, Y$  on  $E$ , by  $\mu_{T(X)}, \mu_{T(Y)}$  the laws of  $T(X), T(Y)$  on  $F$ , and by  $\mu_{(X, T(X))}, \mu_{(Y, T(Y))}$  the joint laws of  $(X, T(X))$  and  $(Y, T(Y))$  on  $E \times F$ . Assume that regular conditional distributions  $\mu_{X|T(X)}(\cdot | \cdot)$  and  $\mu_{Y|T(Y)}(\cdot | \cdot)$  exist.*

Suppose that

$$\mu_{X|T(X)}(\cdot | \cdot) \ll \mu_{Y|T(Y)}(\cdot | \cdot) \quad \text{and} \quad \mu_{T(X)} \ll \mu_{T(Y)}.$$

Then  $\mu_X \ll \mu_Y$  and  $\mu_{(X, T(X))} \ll \mu_{(Y, T(Y))}$ , and for  $\mu_Y$ -a.e.  $e \in E$ ,

$$\frac{d\mu_X}{d\mu_Y}(e) = \frac{d\mu_{(X, T(X))}}{d\mu_{(Y, T(Y))}}(e, T(e)) = \frac{d\mu_{X|T(X)}}{d\mu_{Y|T(Y)}}(e | T(e)) \frac{d\mu_{T(X)}}{d\mu_{T(Y)}}(T(e)).$$

*Proof.* Since  $E$  and  $F$  are Polish spaces, regular conditional distributions  $\mu_{X|T(X)}$  and  $\mu_{Y|T(Y)}$  exist Douc et al. (2018, Appendix).

Let  $\phi : E \times F \rightarrow \mathbb{R}_+$  be a non-negative measurable test function. By disintegration of  $\mu_{(X,T(X))}$  with respect to  $T(X)$ , we have

$$\begin{aligned} \mathbb{E}[\phi(X, T(X))] &= \int_{E \times F} \phi(e, f) d\mu_{(X,T(X))}(e, f) \\ &= \int_F \int_E \phi(e, f) d\mu_{X|T(X)}(e | f) d\mu_{T(X)}(f). \end{aligned}$$

By the assumed absolute continuity of the conditional laws and of the marginals, this can be rewritten as

$$\begin{aligned} \mathbb{E}[\phi(X, T(X))] &= \int_F \int_E \phi(e, f) \frac{d\mu_{X|T(X)}(e | f)}{d\mu_{Y|T(Y)}(e | f)} \frac{d\mu_{T(X)}(f)}{d\mu_{T(Y)}(f)} d\mu_{T(Y)}(f) \\ &= \int_{E \times F} \phi(e, f) \frac{d\mu_{X|T(X)}(e | f)}{d\mu_{Y|T(Y)}(e | f)} \frac{d\mu_{T(X)}(f)}{d\mu_{T(Y)}(f)} d\mu_{(Y,T(Y))}(e, f). \end{aligned}$$

Since this identity holds for all non-negative measurable  $\phi$ , it follows that

$$\mu_{(X,T(X))} \ll \mu_{(Y,T(Y))}$$

and that the Radon–Nikodym derivative is given  $\mu_{(Y,T(Y))}$ -a.e. by

$$\frac{d\mu_{(X,T(X))}}{d\mu_{(Y,T(Y))}}(e, f) = \frac{d\mu_{X|T(X)}(e | f)}{d\mu_{Y|T(Y)}(e | f)} \frac{d\mu_{T(X)}(f)}{d\mu_{T(Y)}(f)}.$$

Let's now consider  $A \in \mathcal{E}$ . We can write

$$\begin{aligned} \mu_X(A) &= \mu_{(X,T(X))}(A \times T(A)) \\ &= \int_{E \times F} \mathbb{1}_{A \times T(A)}(e, f) d\mu_{(X,T(X))}(e, f) \\ &= \int_{E \times F} \mathbb{1}_{A \times T(A)}(e, f) \frac{d\mu_{(X,T(X))}}{d\mu_{(Y,T(Y))}}(e, f) d\mu_{(Y,T(Y))}(e, f) \\ &= \int_E \int_F \mathbb{1}_{A \times T(A)}(e, f) \frac{d\mu_{(X,T(X))}}{d\mu_{(Y,T(Y))}}(e, f) d\mu_{T(Y)|Y}(f | e) d\mu_Y(e) \\ &= \int_E \int_F \mathbb{1}_{A \times T(A)}(e, f) \frac{d\mu_{(X,T(X))}}{d\mu_{(Y,T(Y))}}(e, f) d\delta_{T(e)}(f) d\mu_Y(e) \\ &= \int_E \mathbb{1}_A(e) \frac{d\mu_{(X,T(X))}}{d\mu_{(Y,T(Y))}}(e, T(e)) d\mu_Y(e). \end{aligned}$$

□

**Proposition A.9** (Chain rule for the Kullback–Leibler divergence). *Let  $(E, \mathcal{E})$  and  $(F, \mathcal{F})$  be Polish spaces. Let  $X, Y : (\Omega, \mathcal{A}, \mathbb{P}) \rightarrow (E, \mathcal{E})$  be random variables and let  $T : (E, \mathcal{E}) \rightarrow (F, \mathcal{F})$  be a measurable map.*

*Denote by  $\mu_X, \mu_Y$  the laws of  $X, Y$  on  $E$  and by  $\mu_{T(X)}, \mu_{T(Y)}$  the laws of  $T(X), T(Y)$  on  $F$ . Assume that regular conditional distributions exist and that*

$$\mu_{X|T(X)}(\cdot | \cdot) \ll \mu_{Y|T(Y)}(\cdot | \cdot), \quad \mu_{T(X)} \ll \mu_{T(Y)}.$$

*Then  $\mu_X \ll \mu_Y$  and*

$$D_{\text{KL}}(X||Y) = D_{\text{KL}}(T(X)||T(Y)) + \mathbb{E} \left[ \log \left( \frac{d\mu_{X|T(X)}}{d\mu_{Y|T(Y)}}(X | T(X)) \right) \right].$$

**Algorithm 2** Maximum Sliced Wasserstein

---

**Input:** data samples  $X_0, X_1$ , tolerance  $\text{tol}$   
 $E \sim \mathcal{N}(0, \text{I}_{d-1})$   
 $r = \infty$   
 $\text{old}_{\text{sw}} = 0$   
**while**  $r \geq \text{tol}$  **do**  
      $S^2 := \|E\|^2$   
      $\theta[0] := (S^2 - 1)/(S^2 + 1)$   
     **for**  $i \in \{1, \dots, d-1\}$  **do**  
          $\theta[i] := 2E[i-1]/(S^2 + 1)$   
     **end for**  
      $P_0 = \theta^T X_0$   
      $P_1 = \theta^T X_1$   
      $\text{new}_{\text{sw}} = \text{1d-Wasserstein}(P_0, P_1)$   
      $E = \text{AdamUpdate}(E, \nabla_E \text{new}_{\text{sw}})$   
      $\text{tol} = |\text{new}_{\text{sw}} - \text{old}_{\text{sw}}|$   
**end while**  
**Output:**  $\text{new}_{\text{sw}}, \theta$ .

---

*Proof.* Since  $E$  and  $F$  are Polish spaces, regular conditional distributions  $\mu_{X|T(X)}$  and  $\mu_{Y|T(Y)}$  exist Douc et al. (2018, Appendix). Under the stated absolute continuity assumptions, Lemma A.8 ensures that  $\mu_X \ll \mu_Y$  and that, for  $\mu_X$ -a.e.  $e \in E$ ,

$$\frac{d\mu_X}{d\mu_Y}(e) = \frac{d\mu_{T(X)}}{d\mu_{T(Y)}}(T(e)) \frac{d\mu_{X|T(X)}}{d\mu_{Y|T(Y)}}(e | T(e)).$$

By definition of the Kullback–Leibler divergence,

$$\begin{aligned} \text{D}_{\text{KL}}(X||Y) &= \mathbb{E} \left[ \log \left( \frac{d\mu_X}{d\mu_Y}(X) \right) \right] \\ &= \mathbb{E} \left[ \log \left( \frac{d\mu_{T(X)}}{d\mu_{T(Y)}}(T(X)) \right) \right] + \mathbb{E} \left[ \log \left( \frac{d\mu_{X|T(X)}}{d\mu_{Y|T(Y)}}(X | T(X)) \right) \right] \\ &= \text{D}_{\text{KL}}(T(X)||T(Y)) + \mathbb{E} \left[ \log \left( \frac{d\mu_{X|T(X)}}{d\mu_{Y|T(Y)}}(X | T(X)) \right) \right]. \end{aligned}$$

□

## B. Experiments

### B.1. Synthetic Datasets

**Gaussian Mixture Model.** We consider a 25-component Gaussian Mixture Model (GMM). The two first coordinates of the means of each Gaussian are arranged on a regular  $5 \times 5$  grid spanning  $[-10, 10]^2$ , where each grid point is defined as  $[5i, 5j]$  for  $i, j \in \{-2, \dots, 2\}$ . The other coordinates are set to 0. Each component is characterized by a covariance matrix  $\Sigma = R\Lambda R^T$ , where  $\Lambda$  is a diagonal matrix whose eigenvalues follow the power law  $k^{-3/4}$  for  $k \in \{1, 2, \dots, d\}$ . The orientation is provided by a random rotation matrix  $R$  sampled via the Singular Value Decomposition (SVD) of a standard Gaussian matrix. Mixture weights are independently drawn from a  $\chi_3^2$  distribution and subsequently normalized to sum to one.

**Heavy-Tail.** We consider a heavy-tailed (HT) distribution constructed as a multimodal  $t$ -mixture with  $\nu = 3$  degrees of freedom in dimensions  $d = 40, 100$ . Samples are generated according to

$$W = B T_1 + (1 - B) T_{-1}$$

**Initialization-Aware Score-Based Diffusion Sampling**

Table 5. Comparison of SWD for GMM and HT generated samples across noise levels  $\sigma_T$ .

Model	$\sigma_T = 2$	$\sigma_T = 5$	$\sigma_T = 7$	$\sigma_T = 15$	$\sigma_T = 80$	
<b>GMM</b>						
$d = 40$	$\pi_\infty$	$0.89 \pm 0.05$	$0.49 \pm 0.05$	$0.32 \pm 0.04$	$0.076 \pm 0.003$	$0.11 \pm 0.001$
	$p_0^\theta(x)$	$0.031 \pm 0.002$	$0.1 \pm 0.03$	$0.044 \pm 0.001$	$0.0377 \pm 0.0008$	$0.111 \pm 0.001$
	$\vec{p}_T(x)$	$0.006 \pm 0.0004$	$0.0122 \pm 0.0003$	$0.0161 \pm 0.0004$	$0.038 \pm 0.0006$	$0.109 \pm 0.001$
$d = 100$	$\pi_\infty$	$0.564 \pm 0.009$	$0.279 \pm 0.004$	$0.174 \pm 0.003$	$0.047 \pm 0.001$	$0.0736 \pm 0.0006$
	$p_0^\theta(x)$	$0.049 \pm 0.001$	$0.044 \pm 0.001$	$0.027 \pm 0.0006$	$0.0269 \pm 0.0004$	$0.0744 \pm 0.0004$
	$\vec{p}_T(x)$	$0.0053 \pm 0.0003$	$0.0105 \pm 0.0002$	$0.0136 \pm 0.0003$	$0.028 \pm 0.0003$	$0.0738 \pm 0.0004$
<b>HT</b>						
$d = 40$	$\pi_\infty$	$0.701 \pm 0.010$	$0.403 \pm 0.015$	$0.341 \pm 0.017$	$0.276 \pm 0.024$	$0.259 \pm 0.025$
	$p_0^\theta(x)$	$0.132 \pm 0.021$	$0.179 \pm 0.022$	$0.202 \pm 0.022$	$0.245 \pm 0.025$	$0.258 \pm 0.025$
	$\vec{p}_T(x)$	$0.106 \pm 0.020$	$0.159 \pm 0.022$	$0.187 \pm 0.021$	$0.24 \pm 0.026$	$0.258 \pm 0.025$
$d = 100$	$\pi_\infty$	$0.672 \pm 0.043$	$0.364 \pm 0.056$	$0.312 \pm 0.061$	$0.265 \pm 0.065$	$0.254 \pm 0.067$
	$p_0^\theta(x)$	$0.131 \pm 0.086$	$0.179 \pm 0.072$	$0.203 \pm 0.070$	$0.241 \pm 0.067$	$0.253 \pm 0.067$
	$\vec{p}_T(x)$	$0.111 \pm 0.086$	$0.163 \pm 0.073$	$0.19 \pm 0.071$	$0.236 \pm 0.067$	$0.253 \pm 0.067$

Table 6. Comparison of MaxSWD for GMM and HT generated samples across noise levels  $\sigma_T$ .

Model	$\sigma_T = 2$	$\sigma_T = 5$	$\sigma_T = 7$	$\sigma_T = 15$	$\sigma_T = 80$	
<b>GMM</b>						
$d = 40$	$\pi_\infty$	$5.2 \pm 0.6$	$2.8 \pm 0.1$	$2.1 \pm 0.1$	$0.77 \pm 0.02$	$0.823 \pm 0.01$
	$p_0^\theta(x)$	$0.46 \pm 0.06$	$0.8 \pm 0.07$	$0.49 \pm 0.01$	$0.38 \pm 0.02$	$0.86 \pm 0.01$
	$\vec{p}_T(x)$	$0.1 \pm 0.02$	$0.11 \pm 0.03$	$0.12 \pm 0.02$	$0.39 \pm 0.01$	$0.84 \pm 0.01$
$d = 100$	$\pi_\infty$	$5.03 \pm 0.005$	$2.861 \pm 0.004$	$2.129 \pm 0.005$	$0.88 \pm 0.01$	$0.9 \pm 0.01$
	$p_0^\theta(x)$	$0.97 \pm 0.009$	$0.88 \pm 0.01$	$0.56 \pm 0.01$	$0.4 \pm 0.02$	$0.921 \pm 0.009$
	$\vec{p}_T(x)$	$0.15 \pm 0.04$	$0.15 \pm 0.05$	$0.16 \pm 0.03$	$0.46 \pm 0.01$	$0.921 \pm 0.007$
<b>HT</b>						
$d = 40$	$\pi_\infty$	$0.88 \pm 0.201$	$0.535 \pm 0.222$	$0.49 \pm 0.238$	$0.438 \pm 0.285$	$0.428 \pm 0.287$
	$p_0^\theta(x)$	$0.327 \pm 0.226$	$0.406 \pm 0.212$	$0.443 \pm 0.250$	$0.41 \pm 0.284$	$0.428 \pm 0.287$
	$\vec{p}_T(x)$	$0.402 \pm 0.210$	$0.409 \pm 0.253$	$0.381 \pm 0.253$	$0.414 \pm 0.288$	$0.414 \pm 0.289$
$d = 100$	$\pi_\infty$	$1.265 \pm 1.281$	$0.874 \pm 1.132$	$0.855 \pm 1.137$	$0.792 \pm 1.154$	$0.793 \pm 1.152$
	$p_0^\theta(x)$	$0.586 \pm 1.193$	$0.773 \pm 1.151$	$0.881 \pm 1.127$	$0.787 \pm 1.153$	$0.792 \pm 1.153$
	$\vec{p}_T(x)$	$0.529 \pm 0.849$	$0.725 \pm 1.160$	$0.839 \pm 1.136$	$0.774 \pm 1.154$	$0.792 \pm 1.153$

where where  $B \sim \text{Bernoulli}(1/2)$ , and  $T_{\pm 1} \sim t_\nu(\boldsymbol{\mu}_{\pm 1}, \mathbf{I})$  are multivariate Student-t distributions with  $\nu = 3$  degrees of freedom and location vectors  $\boldsymbol{\mu}_1 = (1/\sqrt{d}, \dots, 1/\sqrt{d})$  and  $\boldsymbol{\mu}_{-1} = (-1/\sqrt{d}, \dots, -1/\sqrt{d})$ . This construction allows us to obtain heavy-tailed marginals and multimodality.

**Training and sampling.** We consider  $\sigma_T \in \{2, 5, 7, 15, 80\}$  for both distributions (HT and GMM) for training and sampling.

In the GMM case, the score function is available; to isolate the contribution of the initialization, we use the exact (ground-truth) score function.  $p_0^\theta(x)$  for this case was obtained by training a RealNVP (Dinh et al., 2017) to solve  $\arg \min_{\theta \in \Theta} D_{\text{KL}}(\vec{p}_T || p_0^\theta)$ . All training details are given in Table 9. For sampling, a 10 steps second order ODE Heun-sampler was used (Karras et al., 2022). For the choice of discretization points, we followed the power law approach from (Karras et al., 2022) with varying values of  $\rho$  as indicated in Figure 5.

In the HT case, we must train a denoiser, since the score function is not analytically available for the convolution of a Gaussian distribution with a heavy-tailed distribution. The training of the denoiser for HT case was performed training a MLP like neural network using training strategies from (Karras et al., 2022). The detail on the denoiser are available in Table 10. For each  $\sigma_T$ , we train a separate denoiser using a training set  $100k$  datapoints.  $p_0^\theta(x)$  is obtained by considering the convolution of a Gaussian distribution with variance  $\sigma_T^2$  and a Student’s  $t$  distribution with parameter  $\hat{\nu}$ . Tail index  $\hat{\nu}$  is estimated per dimension using a multivariate Hill estimator applied to the training set with  $k = 350$ . For sampling, we

**Initialization-Aware Score-Based Diffusion Sampling**

Table 7. Comparison of SWD for initializations of GMM and HT distributions.

	Model	$\sigma_T = 2$	$\sigma_T = 5$	$\sigma_T = 7$	$\sigma_T = 15$	$\sigma_T = 80$
<b>GMM</b>						
$d = 40$	$\pi_\infty$	$0.45 \pm 0.02$	$0.27 \pm 0.01$	$0.23 \pm 0.01$	$0.177 \pm 0.005$	$0.27 \pm 0.01$
	$p_0^\theta(x)$	$0.042 \pm 0.002$	$0.06 \pm 0.01$	$0.041 \pm 0.001$	$0.077 \pm 0.003$	$0.43 \pm 0.02$
	$\vec{p}_T(x)$	$0.0068 \pm 0.0004$	$0.0145 \pm 0.0004$	$0.0199 \pm 0.0005$	$0.042 \pm 0.001$	$0.222 \pm 0.006$
$d = 100$	$\pi_\infty$	$0.219 \pm 0.006$	$0.134 \pm 0.003$	$0.12 \pm 0.003$	$0.111 \pm 0.003$	$0.241 \pm 0.006$
	$p_0^\theta(x)$	$0.0296 \pm 0.0007$	$0.0258 \pm 0.0006$	$0.0317 \pm 0.0008$	$0.057 \pm 0.002$	$0.327 \pm 0.008$
	$\vec{p}_T(x)$	$0.0061 \pm 0.0002$	$0.0141 \pm 0.0003$	$0.0195 \pm 0.0003$	$0.0415 \pm 0.0007$	$0.221 \pm 0.004$
<b>HT</b>						
$d = 40$	$\pi_\infty$	$0.684 \pm 0.009$	$0.328 \pm 0.014$	$0.244 \pm 0.016$	$0.126 \pm 0.016$	$0.217 \pm 0.006$
	$p_0^\theta(x)$	$0.091 \pm 0.024$	$0.101 \pm 0.068$	$0.094 \pm 0.036$	$0.086 \pm 0.031$	$0.216 \pm 0.005$
	$\vec{p}_T(x)$	$0.107 \pm 0.023$	$0.098 \pm 0.025$	$0.095 \pm 0.025$	$0.084 \pm 0.023$	$0.217 \pm 0.007$
$d = 100$	$\pi_\infty$	$0.677 \pm 0.038$	$0.325 \pm 0.056$	$0.244 \pm 0.062$	$0.133 \pm 0.068$	$0.223 \pm 0.018$
	$p_0^\theta(x)$	$0.107 \pm 0.085$	$0.088 \pm 0.075$	$0.085 \pm 0.077$	$0.078 \pm 0.074$	$0.222 \pm 0.017$
	$\vec{p}_T(x)$	$0.131 \pm 0.079$	$0.125 \pm 0.081$	$0.121 \pm 0.081$	$0.109 \pm 0.080$	$0.224 \pm 0.018$

Table 8. Comparison of MaxSWD for initializations of GMM and HT distributions.

	Model	$\sigma_T = 2$	$\sigma_T = 5$	$\sigma_T = 7$	$\sigma_T = 15$	$\sigma_T = 80$
<b>GMM</b>						
$d = 40$	$\pi_\infty$	$5.3 \pm 0.5$	$4.0 \pm 0.3$	$3.3 \pm 0.3$	$1.85 \pm 0.02$	$1.26 \pm 0.09$
	$p_0^\theta(x)$	$0.25 \pm 0.03$	$0.7 \pm 0.3$	$0.39 \pm 0.07$	$0.42 \pm 0.02$	$2.4 \pm 0.09$
	$\vec{p}_T(x)$	$0.026 \pm 0.006$	$0.051 \pm 0.005$	$0.068 \pm 0.008$	$0.14 \pm 0.02$	$0.76 \pm 0.08$
$d = 100$	$\pi_\infty$	$4.884 \pm 0.003$	$3.378 \pm 0.006$	$3.0 \pm 0.2$	$1.9 \pm 0.02$	$1.52 \pm 0.08$
	$p_0^\theta(x)$	$0.44 \pm 0.004$	$0.531 \pm 0.004$	$0.35 \pm 0.05$	$0.45 \pm 0.02$	$2.66 \pm 0.07$
	$\vec{p}_T(x)$	$0.033 \pm 0.004$	$0.073 \pm 0.006$	$0.102 \pm 0.008$	$0.22 \pm 0.01$	$1.16 \pm 0.09$
<b>HT</b>						
$d = 40$	$\pi_\infty$	$0.991 \pm 0.151$	$0.62 \pm 0.249$	$0.534 \pm 0.265$	$0.443 \pm 0.259$	$0.751 \pm 0.080$
	$p_0^\theta(x)$	$0.24 \pm 0.223$	$0.38 \pm 0.707$	$0.253 \pm 0.245$	$0.386 \pm 0.323$	$0.744 \pm 0.084$
	$\vec{p}_T(x)$	$0.33 \pm 0.180$	$0.304 \pm 0.256$	$0.301 \pm 0.274$	$0.418 \pm 0.308$	$0.773 \pm 0.091$
$d = 100$	$\pi_\infty$	$1.243 \pm 1.038$	$0.973 \pm 1.105$	$0.812 \pm 1.138$	$0.807 \pm 1.139$	$1.297 \pm 0.595$
	$p_0^\theta(x)$	$0.525 \pm 1.170$	$0.611 \pm 1.144$	$0.449 \pm 0.859$	$0.71 \pm 1.157$	$1.184 \pm 0.075$
	$\vec{p}_T(x)$	$0.319 \pm 0.195$	$0.504 \pm 0.581$	$0.599 \pm 0.600$	$0.815 \pm 1.076$	$1.252 \pm 0.363$

consider 200 denoising steps and  $\rho = 7$  using the EDM sampler (Karras et al., 2022) for each time horizon  $\sigma_T$ , since our primary objective is to isolate the role of the initialization in tail reconstruction.

**Evaluation.** Evaluation was performed using Sliced Wasserstein Distances (SWD) and maximum Sliced Wasserstein Distances (MaxSWD) for GMM and using SWD, MaxSWD and relative quantile error for the HT case for all noise regimes ( $\sigma_T \in \{2, 5, 7, 15, 80\}$ ) and different initializations ( $\vec{p}_T, p_0^\theta, \pi_\infty$ ). MaxSWD is computed using Algorithm 2, which implements an optimization procedure to identify the maximal sliced Wasserstein distance, improving upon the heuristic grid search approach. The relative error for a quantile is defined as

$$E_{\text{rel}} = \frac{|x_q - \hat{x}_q|}{x_q},$$

where  $x_q$  is the true value of the  $q$ -th quantile and  $\hat{x}_q$  is the corresponding estimated value. This metric provides a normalized measure of the discrepancy between the estimated and true quantile, allowing for a straightforward assessment of quantile reconstruction accuracy.

For the GMM case, three different mixtures were sampled. For each mixture, we train a single flow for initialization and we compute SWD and MaxSWD using 25 comparisons between independent test data and generated samples for each initialization, with  $10^6$  samples per evaluation. SWD was computed using 500 slices, MaxSWD using optimization. The results are then aggregated across different mixture samples obtaining 75 evaluations ( $3 \times 25$ ).

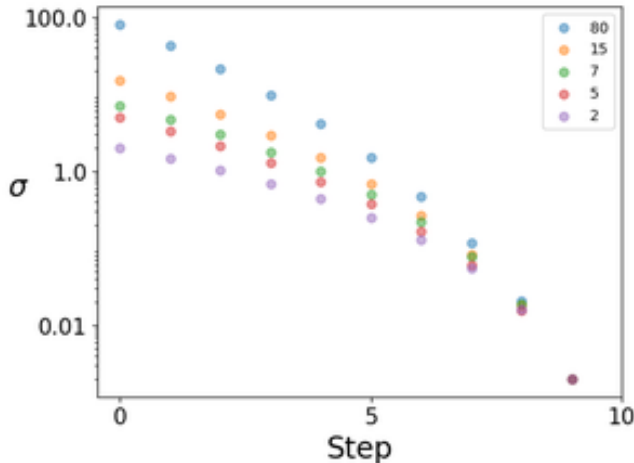


Figure 5. Illustration of different choices of the discretization points for the GMM case.

Table 9. Table of configurations for the training of the Normalizing flow (Dinh et al., 2017) using the Adam optimizer (Kingma and Ba, 2014).

Learning rate	Batch size	Dataset size	N Layers	Layer Width	N Epochs
$10^{-4}$	2048	$5 \times 10^5$	10	1000	100

For the HT case, we train a single denoiser and estimate  $\hat{\nu}$  once. We then compute SWD and MaxSWD using 25 comparisons between independent test data and generated samples for each initialization, with  $10^6$  samples per evaluation. SWD is calculated using 500 slices, MaxSWD using optimization.

Table 5 and 6 summarize the SWD and MaxSWD results for generated data across different time horizons and initialization schemes. We additionally compare the quality of the initializations  $p_0^\theta$  and  $\pi_\infty$  against  $\vec{p}_T$ , using the same number of tests and samples per test. Table 7 and 8 report the SWD and MaxSWD results for the initialization data across different time horizons and initialization schemes. Table 11 reports the reference values of MaxSWD ( $\vec{p}_T$  vs  $\vec{p}_T$ ) using the same number of tests and data per test. For the quantile relative error estimation, we use a dataset of size  $10^7$ . The error is computed for each marginal, and the mean across all dimensions is taken to provide a robust estimation. Table 12 reports the relative quantile errors for  $d = 100$ , all different time horizons  $\sigma_T$  and range of quantiles  $q \in \{0.99, \dots, 0.99999\}$ . Finally, in Figure 6, we present the empirical quantile functions of the first marginal computed on the test data and on data generated from different initializations, estimated using  $10^7$  datapoints.

Table 10. Configuration of the MLP denoiser used for the HT case. The model uses four fully connected blocks with GroupNorm and SiLU activations. The noise schedule is continuous with log-normal sampling. FNet refers to the denoiser of Karras et al. (2022). We use Adam optimizer (Kingma and Ba, 2014).

Learning rate	Batch size	Dataset size	Blocks	Channel Multipliers	Normalization	Activation	Positional Embedding
$10^{-4}$	20,000	$10^5$	4	[2,4,4,2]	GroupNorm	SiLU	FNet-style

## B.2. Images datasets

**Datasets and general context.** Concerning images benchmarks, we tested our approach on FFHQ-64 and two subset of ImageNet-512. We will note  $\text{ImageNet}_{\text{dogs}}$  the subset composed by the 50 randomly selected classes of dogs and we will note  $\text{ImageNet}_{\text{birds}}$  the subset composed by 50 randomly birds classes. We conduct experiments on FFHQ for unconditional generation and on  $\text{ImageNet}_{\text{dogs}}$  and  $\text{ImageNet}_{\text{birds}}$  to evaluate both conditional fidelity to desired classes and robustness across closely related categories.

For FFHQ-64, we used the pretrained model from Karras et al. (2022), in its VE version. For ImageNet, we used the pretrained model from Karras et al. (2024) using the denoiser of size S. The denoiser for ImageNet-512 is trained on

**Initialization-Aware Score-Based Diffusion Sampling**

Table 11. Reference values for the MaxSWD of initialization ( $\vec{p}_T$  vs  $\vec{p}_T$ ) for different time horizons.

$\sigma_T$	(GMM, $d = 40$ )	(GMM, $d = 100$ )	(HT, $d = 40$ )	(HT, $d = 100$ )
0	0.11 ± 0.03	0.13 ± 0.04	0.209 ± 0.268	0.335 ± 0.864
2	0.025 ± 0.004	0.034 ± 0.004	0.286 ± 0.328	0.374 ± 0.862
5	0.049 ± 0.007	0.073 ± 0.006	0.250 ± 0.282	0.660 ± 1.147
7	0.067 ± 0.009	0.104 ± 0.007	0.324 ± 0.321	0.738 ± 1.180
15	0.14 ± 0.02	0.22 ± 0.02	0.363 ± 0.340	0.830 ± 1.157
80	0.76 ± 0.1	1.21 ± 0.08	0.758 ± 0.087	1.321 ± 0.668

Table 12. Tail Precision Comparison (Relative Error) for HT distribution

Quantile $q$	Model	Relative Error (RE) ↓				
		$\sigma_T = 2$	$\sigma_T = 5$	$\sigma_T = 7$	$\sigma_T = 15$	$\sigma_T = 80$
0.99	$\pi_\infty$	0.41 ± 0.01	0.18 ± 0.02	0.13 ± 0.03	0.08 ± 0.03	0.07 ± 0.02
	$p_0^\theta(x)$	0.10 ± 0.03	0.09 ± 0.04	0.08 ± 0.04	0.07 ± 0.03	0.07 ± 0.02
	$\vec{p}_T(x)$	0.11 ± 0.02	0.09 ± 0.03	0.08 ± 0.04	0.07 ± 0.03	0.07 ± 0.02
0.999	$\pi_\infty$	0.58 ± 0.02	0.32 ± 0.06	0.26 ± 0.08	0.18 ± 0.07	0.15 ± 0.04
	$p_0^\theta(x)$	0.07 ± 0.08	0.15 ± 0.10	0.17 ± 0.10	0.16 ± 0.07	0.15 ± 0.04
	$\vec{p}_T(x)$	0.08 ± 0.07	0.17 ± 0.09	0.17 ± 0.09	0.16 ± 0.07	0.15 ± 0.04
0.9999	$\pi_\infty$	0.74 ± 0.01	0.52 ± 0.07	0.45 ± 0.09	0.35 ± 0.10	0.30 ± 0.07
	$p_0^\theta(x)$	0.09 ± 0.09	0.15 ± 0.16	0.21 ± 0.17	0.31 ± 0.11	0.30 ± 0.07
	$\vec{p}_T(x)$	0.05 ± 0.08	0.12 ± 0.16	0.24 ± 0.15	0.31 ± 0.11	0.30 ± 0.07
0.99999	$\pi_\infty$	0.85 ± 0.01	0.69 ± 0.05	0.61 ± 0.08	0.53 ± 0.09	0.50 ± 0.07
	$p_0^\theta(x)$	0.11 ± 0.09	0.24 ± 0.16	0.30 ± 0.16	0.47 ± 0.11	0.50 ± 0.07
	$\vec{p}_T(x)$	0.10 ± 0.07	0.26 ± 0.13	0.32 ± 0.14	0.48 ± 0.10	0.50 ± 0.07

latent representations obtained via Stable VAE (Stability AI, 2025), therefore our short time sampling is performed in the framework of latent representations. For both cases, we used the EDM sampler (Karras et al., 2022).

To implement our approach we use as model for  $p_0^\theta$  the Transformer based Normalizing Flow TarFlow (Zhai et al., 2025). The difference between the original TarFlow model and training and our implementation is summarized in Table 15. Our model is at least 10 times smaller. We trained our model on noised data using short time horizon  $\sigma_T = 7$ . Two training strategies were used for training the model : a fixed one where we used the same noise for all the epochs, as summarized in Algorithm 1 and a dynamical one where at each epoch we add new noise batch to data as summarized in Algorithm 3. Unless otherwise specified, we use the method described in Algorithm 1. When indicated as dynamical, we instead employ the variant defined in Algorithm 3. Although a small amount of noise is often added for stability in classical normalizing flow training, the learning procedure fundamentally relies on fixed data. The first, fixed approach is therefore closer to classical normalizing flow training, whereas the second, dynamical approach aligns more closely with a Monte Carlo approximation of the loss  $\mathbb{E}[-\log p_0^\theta(\vec{X}_0 + \sigma_T Z)]$ .

For both FFHQ and ImageNet, we trained  $p_0^\theta$  using noised data with the noise schedule  $\sigma_T = 7$  described above. Directly training the TarFlow architecture on noised data can be problematic, as it may exceed the original model’s training range (specifically  $[-1, 1]$  for images). We found that dividing the noised data by a *Training Factor* during training, and multiplying by the same factor during sampling initialization, significantly improves generation quality. Additional details on initialization are summarized in Table 15.

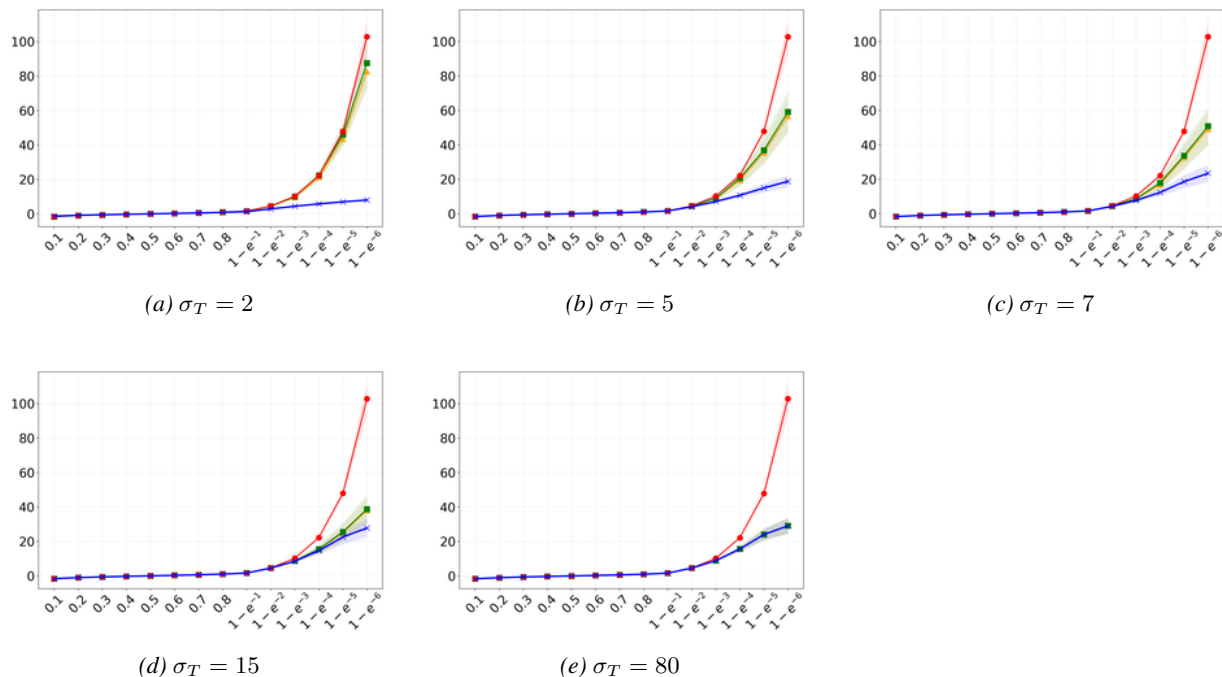


Figure 6. Quantile plot (0.1–0.999999) of mean and std over all dimensions  $d = 100$  of quantile estimation of the heavy-tailed distribution using  $10^7$  samples.  $p_\infty$  in blue,  $p_T$  in orange,  $p_\theta$  in green, real data in red. On the x-axis the quantile levels, on the y-axis the quantile values.

Table 13. Aggregated Results for ImageNet<sub>birds</sub>

Model	FID	DINO FD	KID	SWD	MaxWD
$\pi_\infty(\sigma_T = 80)$ (standard)	5.90	67.13	0.0018	$0.042 \pm 0.001$	$5.095 \pm 0.129$
$p_0^\theta$ - CFG <sub>flow</sub> = 0.5	3.38	58.72	0.0009	$0.016 \pm 0.000$	$1.955 \pm 0.112$
$p_0^\theta$ - CFG <sub>flow</sub> = 1.0	3.30	63.26	0.0009	$0.023 \pm 0.000$	$1.984 \pm 0.041$
$p_0^\theta$ - CFG <sub>flow</sub> = 1.5	3.11	69.58	0.0008	$0.035 \pm 0.000$	$4.781 \pm 0.124$
$p_0^\theta$ - CFG <sub>flow</sub> = 2.0	2.93	79.57	0.0006	$0.048 \pm 0.001$	$6.992 \pm 0.145$
$p_0^\theta$ - CFG <sub>flow</sub> = 0.5 (dynamical)	4.35	59.56	0.0013	$0.027 \pm 0.000$	$2.999 \pm 0.062$
$p_0^\theta$ - CFG <sub>flow</sub> = 1.0 (dynamical)	4.82	65.86	0.0015	$0.028 \pm 0.000$	$3.069 \pm 0.051$
$p_0^\theta$ - CFG <sub>flow</sub> = 1.5 (dynamical)	5.38	72.84	0.0016	$0.031 \pm 0.000$	$3.693 \pm 0.047$
$p_0^\theta$ - CFG <sub>flow</sub> = 2.0 (dynamical)	5.92	81.48	0.0017	$0.035 \pm 0.000$	$4.509 \pm 0.050$
$\tilde{p}_T$	3.91	53.49	0.0011	$0.022 \pm 0.000$	$1.258 \pm 0.633$
$\pi_\infty(\sigma_T = 7)$	4.15	68.42	0.0011	$0.041 \pm 0.000$	$8.174 \pm 0.063$

**Algorithm 3** Short-Horizon Flow-Diffusion Training - Dynamical

- 1: **Input:** Dataset  $\mathcal{D} = \{\mathbf{x}_0^{(i)}\}_{i=1}^N$
- 2: **Output:** Optimized  $p_0^\theta$
- 3: **for** each epoch **do**
- 4:   Noisy dataset  $\mathcal{D}_T = \{\mathbf{x}_0^{(i)} + \sigma_T \mathbf{z}^{(i)}\}_{i=1}^N$   
        $\mathbf{z}^{(i)} \sim \mathcal{N}(0, \mathbf{I})$
- 5:   **for** each training iteration **do**
- 6:     Batch  $\{\mathbf{x}_T\}$  from  $\mathcal{D}_T$
- 7:     Gradient Descent step on  $-\log p_0^\theta(\mathbf{x}_T)$
- 8:   **end for**
- 9: **end for**

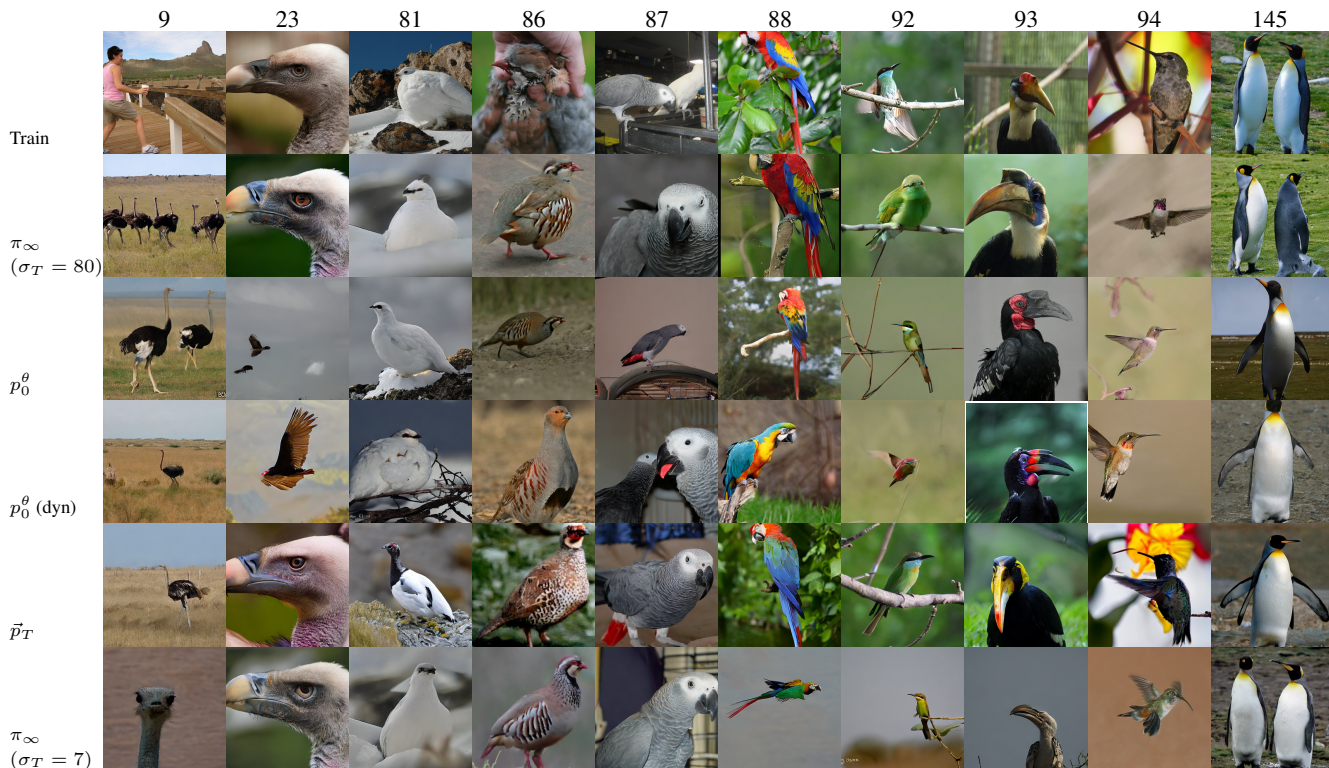
Model	FID	DINO FD	KID	SWD	MaxWD
$\pi_\infty(\sigma_T = 80)$ (standard)	2.53	198.34	0.0013	$0.041 \pm 0.003$	$5.380 \pm 0.282$
$p_0^\theta$	3.00	210.86	0.0019	$0.036 \pm 0.002$	$3.295 \pm 0.331$
$p_0^\theta$ (dynamical)	3.54	221.39	0.0024	$0.062 \pm 0.002$	$6.646 \pm 0.274$
$\vec{p}_T$	2.47	188.70	0.0014	$0.011 \pm 0.001$	$0.085 \pm 0.289$
$\pi_\infty(\sigma_T = 7)$	16.80	322.57	0.0152	$0.255 \pm 0.001$	$25.138 \pm 0.134$

Table 14. Aggregated Results for FFHQ

**Sampling.** For all datasets, we use the EDM sampler and evaluate five different sampling strategies. First, we follow the classical procedure, starting from a Gaussian prior with time horizon  $\sigma_T = 80$ , using 40 steps and  $\rho = 7$  for FFHQ-64 and 32 steps and  $\rho = 7$  for ImageNet-512, as in Karras et al. (2022; 2024). We denote this approach as  $\pi_\infty(\sigma_T = 80)$ . Second, we consider two variants of our initialization-aware short-horizon sampling: in one, we initialize from  $p_0^\theta$  trained in the fixed variant, and in the other, from  $p_0^\theta$  trained in the dynamical variant. We respectively denote these approaches as  $p_0^\theta$  and  $p_0^\theta$  (dynamical). Third, we use a classic Gaussian initialization, but with the short horizon  $\sigma_T = 7$ , denoted  $\pi_\infty(\sigma_T = 7)$ . Finally, we consider short-horizon sampling initialized from the empirical training distribution convolved with Gaussian noise of level  $\sigma_T = 7$ , denoted  $\vec{p}_T$ . For conditional initialization on the ImageNet subset, we employ class-conditional sampling with a weight  $\text{CFG}_{\text{flow}}$  ranging from 0.5 to 2, as implemented in the standard TarFlow model. For the denoiser, we use the standard  $\text{CFG}_{\text{SGM}}$  weight of 1.9, following (Karras et al., 2024). For initializations starting from  $\sigma_T = 7$ , we consistently employ 20 denoising steps and  $\rho = 5$ . Across  $\rho$  values the sampling quality remains stable.

Table 15. TarFlow (Zhai et al., 2025) configurations of original model and the model we use for initialization.

Model	Channel size	Number of blocks	Layers per block	Epochs	Batch size	Learning Rate	Training Factor	Guidance
Original Model	512	8	8	100	128 (default)	$1e - 4$ (default)	not implemented	0 for uncond/1 for cond (default)
$p_0^\theta$ for FFHQ	128	1	8	700	500	$3e - 4$	14	0 (uncond)
$p_0^\theta$ for ImageNet <sub>birds</sub>	128	1	8	700	1000	$3e - 4$	14	0.5 - 2 (cond)
$p_0^\theta$ for ImageNet <sub>dogs</sub>	128	1	8	700	1000	$3e - 4$	14	0.5 - 2 (cond)


 Figure 7. Grid comparison for ImageNet<sub>birds</sub> generation.

**Metrics and Evaluation.** We evaluated our approach using several metrics. First, we consider Fréchet Inception Distance (FID) (Heusel et al., 2017) to evaluate generation quality. Recent research has highlighted limitations of FID (Jayasumana et al., 2023; Stein et al., 2023); therefore, we also consider other metrics to assess sample quality. These include the unbiased Kernel Inception Distance (KID) (Bińkowski et al., 2018), Dino Fréchet Distance (DinoFD), which follows the same approach as FID but uses a newer model for feature extraction (Oquab et al., 2024; Stein et al., 2023; Karras et al., 2024), Sliced Wasserstein Distance (SWD), and Max Sliced Wasserstein Distance (MaxSWD). For ImageNet-512, they are computed in latent space. While FID, KID, and similar metrics assess realism of generated images, Wasserstein metrics evaluate the fidelity of the underlying probabilistic distribution, which is crucial when realistic appearance is not the main objective. Wasserstein metrics on ImageNet are performed in latent space. For each dataset (FFHQ-64, ImageNet<sub>dogs</sub>, ImageNet<sub>birds</sub>), we trained two TarFlow model for  $p_0^\theta$  (one for Algorithm 1 and one for Algorithm 3) and for each sampling method described, we perform 3 independent generations. For each run, we compute FID, KID, and DinoFD using  $5 \times 10^4$

 Table 16. Aggregated Results for ImageNet<sub>dogs</sub>

Model	FID	DINO FD	KID	SWD	MaxWD
$\pi_\infty(\sigma_T = 80)$ (standard)	10.46	95.30	0.0050	$0.040 \pm 0.001$	$3.739 \pm 0.088$
$p_0^\theta$ - CFG <sub>flow</sub> = 0.5	5.53	70.35	0.0022	$0.029 \pm 0.001$	$2.911 \pm 0.073$
$p_0^\theta$ - CFG <sub>flow</sub> = 1.0	5.25	69.59	0.0021	$0.034 \pm 0.001$	$3.034 \pm 0.071$
$p_0^\theta$ - CFG <sub>flow</sub> = 1.5	4.76	70.36	0.0018	$0.041 \pm 0.001$	$4.359 \pm 0.171$
$p_0^\theta$ - CFG <sub>flow</sub> = 2.0	4.25	71.51	0.0014	$0.050 \pm 0.001$	$6.146 \pm 0.175$
$p_0^\theta$ - CFG <sub>flow</sub> = 0.5 (dynamical)	6.66	73.08	0.0029	$0.033 \pm 0.001$	$2.810 \pm 0.068$
$p_0^\theta$ - CFG <sub>flow</sub> = 1.0 (dynamical)	7.44	76.88	0.0033	$0.034 \pm 0.001$	$2.771 \pm 0.058$
$p_0^\theta$ - CFG <sub>flow</sub> = 1.5 (dynamical)	8.10	81.47	0.0036	$0.035 \pm 0.000$	$2.882 \pm 0.054$
$p_0^\theta$ - CFG <sub>flow</sub> = 2.0 (dynamical)	8.69	87.11	0.0039	$0.038 \pm 0.000$	$3.816 \pm 0.060$
$\bar{p}_T$	6.55	68.93	0.0030	$0.024 \pm 0.000$	$0.376 \pm 0.665$
$\pi_\infty(\sigma_T = 7)$	7.20	85.17	0.0028	$0.034 \pm 0.000$	$7.287 \pm 0.072$



Figure 8. Grid comparison for FFHQ generation.

generated samples and we report the minimum on 3 experiments. For each of 3 experiments, we computed 4 times SWD and MaxSWD using for each test  $17, 5 \times 10^3$  datapoints and  $2 \times 10^4$  slices. We report the global mean and standard deviation for SWD and MaxSWD over the 12 evaluations ( $3 \times 4$ ). We compare generated samples to the training data. These procedures are directly inherited from (Karras et al., 2022; 2024) to maintain fidelity to the original approach.

In Table 14 you can find the aggregated results for FFHQ-64. In Table 13 you can find the aggregated results for ImageNet<sub>birds</sub>. In Table 16 you can find the aggregated results for ImageNet<sub>dogs</sub>. In Figures 7,8 and 9 we report random samples from different datasets. The images shown were obtained by selecting a training sample and, for each generated dataset, finding its nearest neighbor according to the  $L^2$  norm. The labels used follow the order of <https://deeplearning.cms.waikato.ac.nz/user-guide/class-maps/IMAGENET/>. For the ImageNet subsets, the distance was computed in latent space.

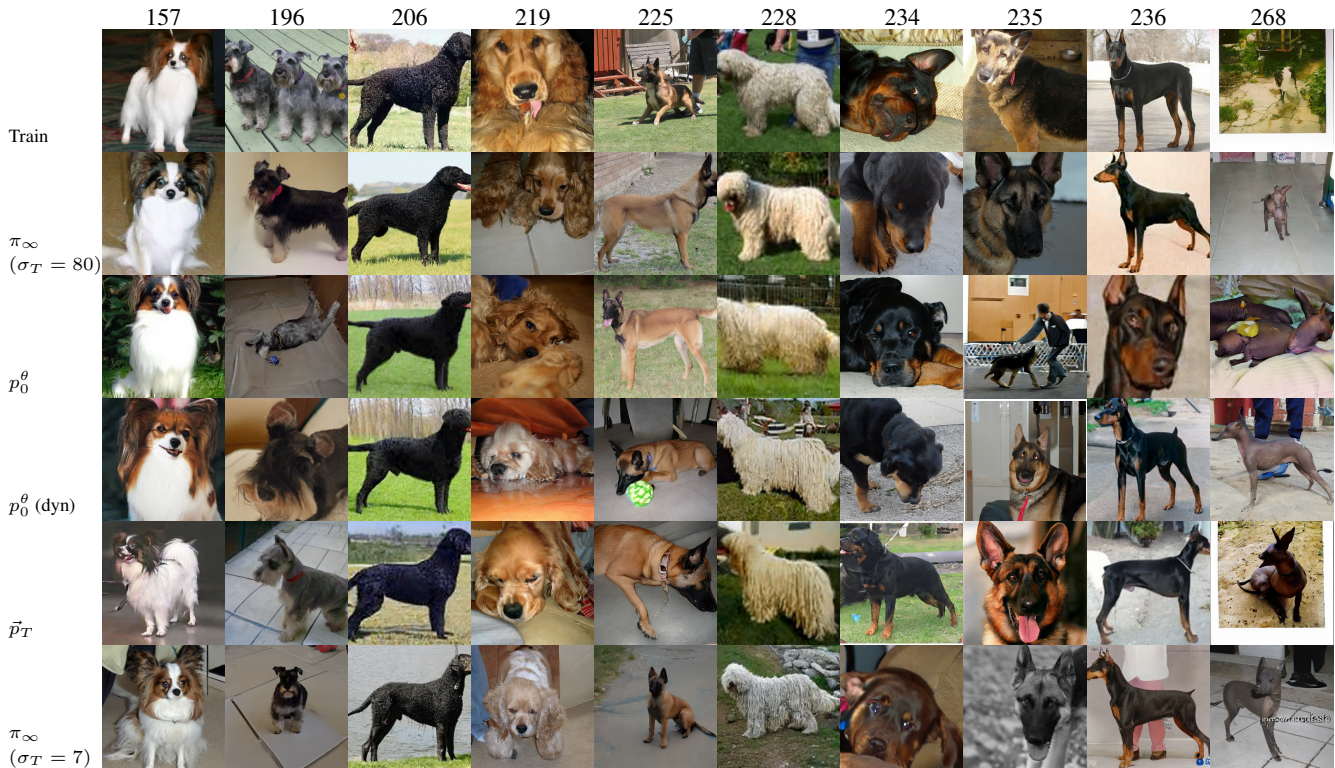


Figure 9. Grid comparison for ImageNet<sub>dogs</sub> generation.

**Results on Image Datasets.** Across all datasets (FFHQ-64, ImageNet<sub>dogs</sub>, ImageNet<sub>birds</sub>), our results show that the proposed short-horizon sampling strategies achieve competitive performance compared to classical long-horizon sampling  $\pi_\infty(\sigma_T = 80)$ .

The  $\vec{p}_T$  approach consistently attains the lowest metrics across all datasets, highlighting the benefit of initializing using the appropriate noised distribution.

For FFHQ-64, the fixed and dynamical  $p_0^\theta$  variants exhibit slightly higher FID and DINO FD than the standard approach, yet remain within a reasonable range, confirming the viability of initialization-aware short-horizon sampling. SWD and MaxWD indicate superior performance of  $p_0^\theta$  for this dataset. On ImageNet<sub>dogs</sub> and ImageNet<sub>birds</sub>, conditional sampling with  $p_0^\theta$  shows clear improvements over standard Gaussian initialization across FID, KID, DINO FD and SWD metrics, emphasizing the strong potential of our method.

Dynamical variants in all datasets exhibit slightly worse results, reflecting that, although the dynamical loss provides a more accurate Monte Carlo estimate, the architecture is not fully able to leverage this advantage. Results of short horizon Gaussian initialization ( $\pi_\infty - \sigma_T = 7$ ) in conditional sampling shows that the fact of using  $\sigma_T = 80$  as a standard is an arbitrary choice that does not suit all datasets, highlighting the importance of initialization-aware strategies. Randomly sampled nearest-neighbor images show that our method produces diverse results and does not simply replicate the training data. Overall, these results indicate that our short-horizon approaches—both fixed and dynamical—produce high-quality samples closely matching the distribution. This approach provide a practical alternative in settings with computational constraints without sacrificing quality and offer a potential alternative in cases where the classical long-horizon approach fails to achieve better results.

### C. Error estimation for $D_{\text{KL}}(\vec{p}_T \| p_0^\theta)$

The goal of this section is to establish conditions to bound the initialization error  $D_{\text{KL}}(\vec{p}_T \| p_0^\theta)$  and following the general logic of (Tang and Yang, 2021)[Theorem 3]. To do so, we start by defining

$$m : \Theta \times \mathbb{R}^d \ni (x, \theta) \rightarrow m(x; \theta) := \log \vec{p}_T(x) - \log p_0^\theta(x) \in \mathbb{R}, \quad (34)$$

and

$$\hat{\theta}^n \in \arg \min_{\theta \in \Theta} \sum_{i=1}^n -\log p_0^\theta(\vec{X}_T^i) = \arg \min_{\theta \in \Theta} n^{-1} \sum_{i=1}^n m(\vec{X}_T^i; \theta), \quad (35)$$

$$\theta^* \in \arg \min_{\theta \in \Theta} D_{\text{KL}}(\vec{p}_T \| p_0^\theta) = \arg \min_{\theta \in \Theta} \mathbb{E} \left[ m(\vec{X}_T; \theta) \right], \quad (36)$$

where  $\Theta$  is a subset of  $\mathbb{R}^{d_\theta}$ . We now restrict our attention to  $p_0^\theta$  of the type normalizing flow (Rezende and Mohamed, 2015), namely, we introduce measure defined by a density  $u(x)$  with respect to  $\lambda_{\mathbb{R}^d}$  and a function

$$T : \mathbb{R}^d \times \Theta \ni (x, \theta) \rightarrow T_\theta(x) \in \mathbb{R}^d, \quad (37)$$

such that for all  $\theta \in \Theta$ ,  $T_\theta : \mathbb{R}^d \rightarrow \mathbb{R}^d$  is an invertible transformation and that  $p_0^\theta$  coincides with the density of the measure induced by the composition that we note  $T_{\theta \# u}$ . In this case, by the change of variables formula, we have that

$$\log p_0^\theta(x) = \log u(T_\theta^{-1}(x)) - \log(\det J_{T_\theta}(x)). \quad (38)$$

Note that this is indeed a simplified framework than the one from (Tang and Yang, 2021), where we consider the encoder and decoder as  $T_\theta^{-1}$  and  $T_\theta$  and the prior as  $u$ . Given a random variable  $X$ , we introduce the Orlicz norm  $\|X\|_{\psi_1}$  (also known as the  $\psi_1$ -norm) as:

$$\|X\|_{\psi_1} = \inf \left\{ K > 0 : \mathbb{E} \left[ \exp \left( \frac{|X|}{K} \right) \right] - 1 \leq 1 \right\}, \quad (39)$$

assumption 3.3 requires the log-density  $\log p_0^\theta(x)$  to be Lipschitz continuous with respect to the parameter  $\theta \in \Theta$  and the Lipschitz constant  $b(x)$  to have a finite first order Orlicz norm under the law of  $\vec{X}_T$ . assumption 3.3 requires the function to be bounded in the Orlicz norm under the supremum over the parameter space. Under assumptions on the loglikelihood we can show that assumption 3.2 implies assumption 3.3, as stated in the following lemma.

**Lemma C.1.** *If there exists  $\theta_0 \in \Theta$  such that  $T_{\theta_0}(x) = x$  for all  $x \in \mathbb{R}^d$  and  $(\alpha, \beta) \in \mathbb{R}_{\geq 0}^2$  such that*

$$\left| \log \frac{\vec{p}_T(x)}{u(x)} \right| \leq \alpha |x| + \beta, \quad (40)$$

*then, assumption 3.3 implies assumption 3.2 with  $D = \alpha \left\| \vec{X}_T \right\|_{\psi_1} + \frac{\beta}{\log 2} + \text{Diam}(\Theta) \left\| b(\vec{X}_T) \right\|_{\psi_1}$ .*

*Proof.* By assumption 3.3, we have that for all  $\theta \in \Theta$  and  $x \in \mathbb{R}^d$ ,

$$|m(x; \theta) - m(x; \theta_0)| \leq \text{Diam}(\Theta) b(x) + |m(x; \theta_0)|, \quad (41)$$

which implies that  $\left\| \sup_{\theta \in \Theta} |m(\vec{X}_T; \theta)| \right\|_{\psi_1} \leq \left\| |m(\vec{X}_T; \theta_0)| \right\|_{\psi_1} + \text{Diam}(\Theta) \left\| b(\vec{X}_T) \right\|_{\psi_1}$ .

But as  $|m(x; \theta_0)| = \left| \log \frac{\vec{p}_T(x)}{u(x)} \right|$ , we have that  $\left\| |m(\vec{X}_T; \theta_0)| \right\|_{\psi_1} \leq \alpha \left\| \vec{X}_T \right\|_{\psi_1} + \frac{\beta}{\log 2}$ .  $\square$